JOURNAL OF GEOPHYSICAL RESEARCH, VOL. 112, B10207, doi:10.1029/2006JB004456, 2007

A probabilistic damage model of stress-induced permeability anisotropy during cataclastic flow

Wenlu Zhu,[1] Laurent G. J. Montési,[1] and Teng-fong Wong[2]

Received 19 April 2006; revised 31 January 2007; accepted 2 August 2007; published 20 October 2007.

[1] A fundamental understanding of the effect of stress on permeability evolution is important for many fault mechanics and reservoir engineering problems. Recent laboratory measurements demonstrate that in the cataclastic flow regime, the stress-induced anisotropic reduction of permeability in porous rocks can be separated into 3 different stages. In the elastic regime (stage I), permeability and porosity reduction are solely controlled by the effective mean stress, with negligible permeability anisotropy. Stage II starts at the onset of shear-enhanced compaction, when a critical yield stress is attained. In stage II, the deviatoric stress exerts primary control over permeability and porosity evolution. The increase in deviatoric stress results in drastic permeability and porosity reduction and considerable permeability anisotropy. The transition from stage II to stage III takes place progressively during the development of pervasive cataclastic flow. In stage III, permeability and porosity reduction becomes gradual again, and permeability anisotropy diminishes. Microstructural observations on deformed samples using laser confocal microscopy reveal that stress-induced microcracking and pore collapse are the primary forms of damage during cataclastic flow. A probabilistic damage model is formulated to characterize the effects of stress on permeability and its anisotropy. In our model, the effects of both effective mean stress and differential stress on permeability evolution are calculated. By introducing stress sensitivity coefficients, we propose a first-order description of the dependence of permeability evolution on different loading paths. Built upon the micromechanisms of deformation in porous rocks, this unified model provides new insight into the coupling of stress and permeability.

Citation: Zhu, W., L. G. J. Montési, and T.-f. Wong (2007), A probabilistic damage model of stress-induced permeability anisotropy during cataclastic flow, *J. Geophys. Res.*, *112*, B10207, doi:10.1029/2006JB004456.

1. Introduction

[2] The transport properties of crustal rocks depend strongly on porosity and pore geometry [*Walsh*, 1965; *Simmons and Richter*, 1976; *Gangi*, 1979; *Shankland et al.*, 1981; *Heard and Page*, 1982]. Many mechanical and chemical processes can substantially alter pore space, and thus affect permeability. Hence a better understanding of many geological processes requires quantitative knowledge of how permeability and its anisotropy evolve during deformation. However, measuring permeability in an active tectonic environment is often difficult because permeability varies significantly among geomaterials and is sensitive to pressure, temperature and stress [e.g., *Brace*, 1980]. Laboratory measurements of the evolution of permeability under crustal pressure, temperature and stress conditions provide useful constraints on these problems [e.g., *Zhu and Wong*, 1997].

[3] Laboratory studies have shown that permeability can be significantly modified under the application of hydrostatic or non-hydrostatic stresses [e.g., *David et al.*, 1994; *Zhu and Wong*, 1997; *Zhang et al.*, 1999]. While an increase in mean stress generally results in porosity reduction and permeability decrease, the effect of deviatoric stress on both deformation and permeability evolution is more complex. In low porosity rocks (with porosities <5% or so), stress-induced dilatancy and permeability enhancement are observed whether the rock fails by brittle faulting or cataclastic flow [e.g., *Zoback and Byerlee*, 1975; *Stormont and Daemen*, 1992; *Zhang et al.*, 1994; *Kiyama et al.*, 1996; *Peach and Spiers*, 1996; *Zhu and Wong*, 1999]. In contrast, in porous rocks (with porosities >5%), it has been shown that under overall compressive loading, a deviatoric stress can either induce dilation by brittle fracture or compaction by cataclastic flow, dependent upon the magnitude of confinement [e.g., *Wong et al.*, 1997]. The dependence of permeability on porosity and deformation mechanism in high-porosity rocks is fundamentally different from that in low-porosity rocks [e.g., *Mordecai and Morris*, 1971; *Holt*, 1989; *Rhett and Teufel*, 1992; *Zhu and Wong*, 1997]. For highly porous rocks, an appreciable amount of permeability reduction is observed with concurrent porosity increase in

[1]Department of Geology and Geophysics, Woods Hole Oceanographic Institution, Woods Hole, Massachusetts, USA.
[2]Department of Geosciences, State University of New York at Stony Brook, Stony Brook, New York, USA.

0148-0227/07/2006JB004456$09.00

the brittle faulting regime [*Zhu and Wong*, 1997; *Main et al.*, 2001], whereas, in the cataclastic flow regime, significant porosity reduction with concomitant permeability decrease is generally observed instead [e.g., *Zhu and Wong*, 1997]. Therefore depending upon rock lithology, the permeability structure and consequently the fluid flow in an active geologic setting can be very different during tectonic deformation [e.g, *Wong and Zhu*, 1999].

[4] Because permeability is a second-rank tensor, permeability anisotropy is expected in a rock subjected to an anisotropic stress field. Yet, in most theoretical models to date, permeability is commonly prescribed as a scalar quantity [e.g., *Person et al.*, 1996; *Ingebritsen and Sanford*, 1998; *Andrews*, 2002; *Segall and Rice*, 2006]. The lack of knowledge about permeability anisotropy, especially in relation to nonhydrostatic loading, is aggravated by the difficulty to measuring simultaneously fluid transport in several different directions at elevated pressures.

[5] To address this problem, *Zhu et al.* [2002] conducted a series of permeability measurements using a new triaxial compression loading configuration — *hybrid compression*. The loading path of a hybrid compression test is designed to ensure that its mean and differential stress history (corresponding to the first and second stress invariants, respectively) coincides with that of a conventional extension test with the same confining pressure. While permeability is measured along the axial direction in both the compression and conventional extension tests, fluid flow is along the maximum principal stress direction in the former case and the minimum principal stress direction in the latter case. Therefore the comparison of permeability values from these two types of tests provides a quantitative estimate of the development of stress-induced permeability anisotropy.

[6] Using this novel loading strategy, *Zhu et al.* [2002] conclude that considerable stress-induced permeability anisotropy exists in porous sandstones deformed in the cataclastic flow regime. Generally, the permeability for flow parallel to the maximum compression direction is greater than that perpendicular to the maximum compression direction as a rock undergoes shear-enhanced compaction. In addition, as the strain increases, the maximum and minimum permeability components gradually converge. While the experimental results from *Zhu et al.* [2002] provide the first systematic observations of anisotropic development of permeability as a function of stress, to extrapolate the data to a specific geological setting requires a deeper understanding of the micromechanics of the process.

[7] To estimate permeability under natural conditions, it is desirable to formulate theoretical relationships between permeability, porosity, stress and cumulative strain [e.g., *Paterson*, 1983; *Walsh and Brace*, 1984; *Bourbie and Zinszner*, 1985; *David et al.*, 1994; *Ngwenya et al.*, 2003; *Morris et al.*, 2003]. As permeability is closely related to pore space, great efforts have been made to relate permeability to porosity. A generalized power law relationship between permeability and porosity is widely adopted, with the power law exponent sensitively dependent on pore volume, pore geometry and pore connectivity [e.g., *David et al.*, 1994; *Bernabé et al.*, 2003]. However, to date, few models quantify the effect of deviatoric stress on permeability [e.g., *Zhu*, 2006].

[8] For hydrostatic compaction, *David et al.* [1994] approximated compaction-induced permeability reduction before failure by an exponential function between permeability and effective mean stress. In their model, a pressure sensitivity coefficient of permeability during hydrostatic mechanical compaction was proposed. Review of laboratory data indicates that the sensitivity of permeability to mean stress varies widely among geomaterials [e.g., *David et al.*, 1994], with materials of high pressure sensitivity having a greater potential for development of significant pore pressure excess. The exponential model enables us to use laboratory data to constrain the likelihood of excess pore pressure generation and maintenance in specific lithological settings [*Wong and Zhu*, 1999].

[9] Nonhydrostatic stress is ubiquitous in active tectonic environments. Based on experimental data on permeability evolution during non-hydrostatic mechanical compaction, *Zhu* [2006] formulates a cumulative damage model to quantify the influence of deviatoric stress on permeability reduction associated with compactive cataclastic flow. It is well recognized that in the cataclastic flow regime, although the failure mode is macroscopically "ductile", the microscopic deformation mechanism involves pervasive brittle cracking [*Wong et al.*, 1992]. The significant permeability reduction in porous rocks undergoing shear-enhanced compaction is caused by microcracking-facilitated grain crushing and pore collapse [e.g., *Zhu and Wong*, 1997]. *Zhu* [2006] demonstrates that damage in the form of microcracking at a given mean stress can be approximated by a Gaussian function, and the macroscopic permeability reduction during cataclastic flow can be quantified using an error function. This micromechanics-based probabilistic damage model captures the drastic permeability reduction that results from grain crushing and pore collapse in porous rocks in the cataclastic flow regime [*Zhu*, 2006]. In this study, we address the development of permeability anisotropy as well as permeability reduction upon cataclastic failure.

[10] Quantitative characterization of damage has demonstrated that deviatoric stresses can induce significant anisotropy in microcrack density, due to the preferential development of stress-induced cracking subparallel to the maximum principal stress σ_1 [e.g., *Menéndez et al.*, 1996]. The permeability tensor is clearly sensitive to the geometric complexity of the pore space. Hence permeability anisotropy is expected as stress-induced microcracking is pervasive during shear-enhanced compaction. However, a quantitative relationship between microscopic processes and macroscopic physical properties remains elusive. Can the probabilistic model be used to quantify stress-induced permeability anisotropy associated with compactive cataclastic flow? Can the model capture the transient nature of permeability anisotropy observed in the laboratory experiments [e.g., *Zhu et al.*, 2002]? A model that quantifies successfully the influences of loading path and stress state on permeability anisotropy will provide the necessary link between laboratory data and large scale geological problems. With these questions in mind, the focus of this study is to provide quantitative constraints on the stress sensitivity of permeability anisotropy during compactive cataclatic flow.

2. Review of Experimental Results

[11] Experimental data of the evolution of permeability anisotropy during shear-enhanced compaction are scarce. In

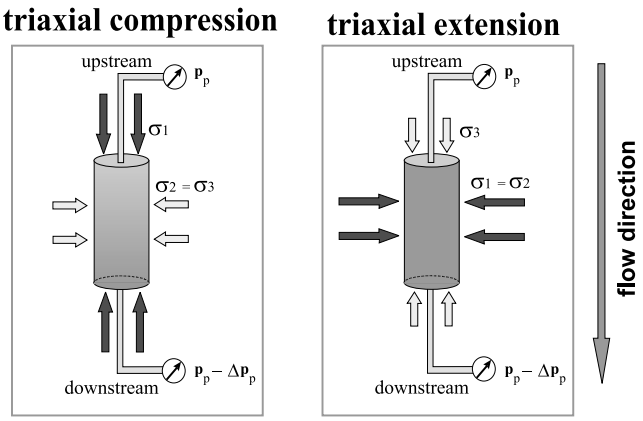

Figure 1. Schematic diagram of the triaxial experimental setup. Because the axial stress is applied separately by a servo-controlled hydraulic system while the lateral stresses are applied by an air-driven pump, deformation tests can be conducted under both triaxial compression and extension conditions. A wide-range permeameter is included, which is designed to use either the steady state flow or pulse transient technique for permeability measurements.

this study, we focus on the data sets reported by *Zhu and Wong* [1997] (for conventional triaxial compression), *Zhu et al.* [1997] (for conventional triaxial extension) and *Zhu et al.* [2002] (for hybrid triaxial compression). The hybrid compressional loading configuration is crucial for characterizing stress-induced permeability anisotropy in these studies. As neither the extension nor the hybrid compression tests are common practice, we describe in this section the loading configurations in some details. Then, a subset of previously published experimental data [*Zhu and Wong*, 1997; *Zhu et al.*, 1997, 2002] is presented to illustrate the synopsis of permeability evolution as a function of stress. Comparison of the permeability data obtained under different loading paths demonstrates how permeability anisotropy evolves during cataclastic flow. More complete data sets and detailed discussion of both the mechanical and permeability behaviors can be found in *Zhu and Wong* [1997] and *Zhu et al.* [1997, 2002].

2.1. Experimental Setup

[12] Schematic diagrams of triaxial compression and extension experiments are shown in Figure 1. We conducted hydromechanical tests on various porous sandstones with initial porosity ranging from 15% to 35% using either compression or extension loading configurations [see *Zhu and Wong*, 1997; *Zhu et al.*, 1997, 2002]. In each test, the jacketed cylindrical sample was saturated with distilled water and deformed at room temperature. Kerosene and distilled water were used as confining medium and pore fluid, respectively. All of the experiments were conducted with a fixed pore pressure (P_p) of 10 MPa, under confining pressures ranging from 13 to 550 MPa. The confining pressure and the pore pressure were monitored by strain gauge pressure transducers with accuracies of 0.5 and 0.125 MPa, respectively. The axial load was provided by a servo-controlled hydraulic ram operated separately from the confining pressure pump and was measured by an external load cell with an accuracy of 1 kN.

[13] Stress-induced permeability and porosity changes were measured during compaction. Adjustment of a pore pressure generator (volumometer) kept the pore pressure constant, and the pore volume change was recorded by monitoring the piston displacement of the volumometer with a displacement transducer (DCDT). The porosity change was calculated from the ratio of the pore volume change to the initial bulk volume of the sample with an uncertainty of 0.1%. Axial displacement was monitored by a DCDT mounted on the loading piston. A nominal strain rate of 2×10^{-5}/s was used to ensure fully drained conditions. A wide range permeameter was used to measure permeability during deformation. Two different techniques—steady state flow (for permeability $>10^{-16}$ m^2) and pulse transient (for permeability $<10^{-16}$ m^2) methods—were implemented according to the magnitude of permeability [e.g., *Bernabé*, 1987]. Mechanical loading was stopped at different stages of deformation so that in situ permeability was measured as a function of the stress state. The average "holding" period was ~3 h, during which stress relaxation was observed. The uncertainty of permeability measurements is less than 15%. A more detailed description of this system can be found in *Zhu and Wong* [1997].

2.2. Loading Configuration

[14] Unlike metals and low porosity rocks, for which the inelastic and failure behaviors are primarily controlled by the deviatoric stress, the mechanical deformation of a porous rock depends also on the mean stress. Hence the constitutive descriptions of the mechanical behavior and permeability evolution in an isotropic, porous rock must involve at least the first and second invariants of the stress tensor. It is commonly assumed in rock and soil mechanics that the dependence on the third invariant can be neglected in such constitutive models [e.g., *Mogi*, 1968]. In an axisymmetric loading configuration, where the intermediate principal stress σ_2 is equal to either the maximum principal stress σ_1 or the minimum principal stress σ_3, the first and second stress invariants are simply related to the effective mean stress $P = (\sigma_1 + \sigma_2 + {}_3)/3 - P_p$ and differential stress $Q = \sigma_1 - \sigma_3$, respectively. The stress history in a triaxial test is therefore represented by a trajectory in P-Q space, which will be referred to as the "loading path" in later discussions.

[15] To characterize the stress-induced permeability anisotropy of Ottawa sand, *Zoback and Byerlee* [1976] proposed a method of comparing data on permeability evolution during conventional triaxial compression and extension tests. In both loading configurations, the minimum principal stress σ_3 is maintained constant. In a conventional triaxial compression test the maximum principal stress σ_1 is applied parallel to the axial direction ($\sigma_1 > \sigma_2 = \sigma_3$), whereas in a conventional triaxial extension test, σ_1 is along the radial direction ($\sigma_1 = \sigma_2 > \sigma_3$). While permeability is always measured in the axial direction, it is parallel to σ_1 in the former case and perpendicular to σ_1 in the latter case. Stress-induced permeability anisotropy was inferred by comparing permeability data obtained in triaxial compression tests (k_1) to those measured in extension tests (k_3). A similar methodology was adopted by *Bruno* [1994]

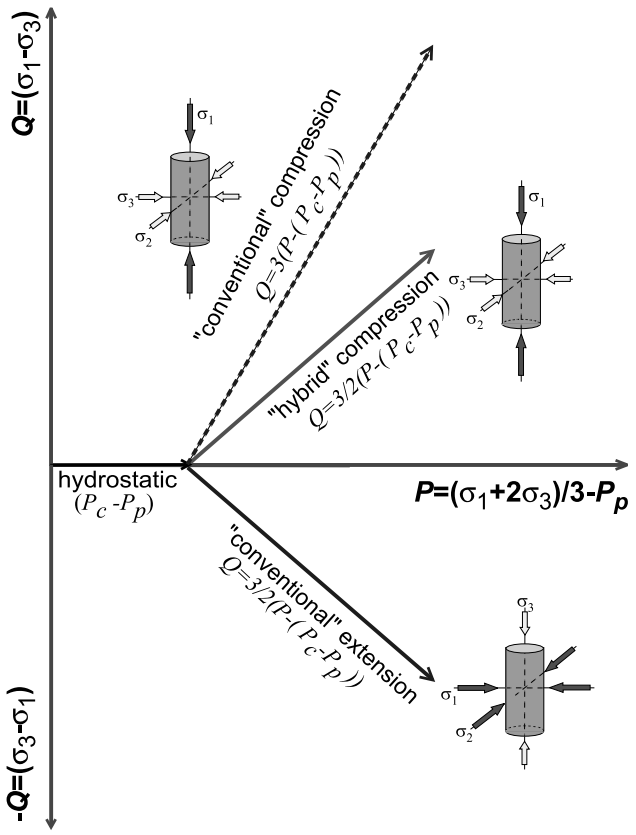

Figure 2. Comparison of loading paths between conventional triaxial compression, conventional triaxial extension and hybrid triaxial compression tests, in *P*-*Q* space. Note that the loading paths of conventional extension and compression tests have at most one coincident stress state, but the loading paths of conventional extension and hybrid compression tests coincide. Permeability values obtained in conventional extension and hybrid compression tests thus provide more meaningful comparison for stress-induced anisotropy.

and *Zhu et al.* [1997] to study the evolution of permeability anisotropy in porous sandstones deformed in the brittle faulting and cataclastic flow regimes, respectively.

[16] However, because the intermediate principal stress σ_2 equals σ_3 in a conventional compression test but equals σ_1 in a conventional extension test, the loading paths in these two cases do not coincide (Figure 2). Because deformation in these tests strongly depends on loading history, inevitable ambiguity is introduced when characterizing permeability anisotropy in porous rocks using the foresaid methodology [*Zhu et al.*, 1997].

[17] Ideally, permeability anisotropy should be inferred from data for flow along different principal directions in tests with identical loading paths. To obtain a loading path of a compressional test that is identical to that of a conventional triaxial extension test, one needs to adjust σ_3 (and σ_2) in the compression test systematically to follow the desired loading path (instead of $\sigma_2 = \sigma_3$ being constant as in a conventional compression test). Such tests along the prescribed loading path are referred as "hybrid" triaxial compression tests [*Zhu et al.*, 2002]. Laboratory methods for deforming rocks using the three loading configurations are briefly described below.

2.2.1. Conventional Triaxial Compression

[18] Conventional triaxial compression is the most used configuration in conducting laboratory deformation tests. In such a test, the sample is first loaded hydrostatically to a desired confining pressure P_c and pore pressure P_p. Non-hydrostatic deformation is achieved by increasing the axial stress σ_1 using a servo-controlled hydraulic ram, while maintaining the lateral stresses constant ($\sigma_2 = \sigma_3 = P_c$). The loading path of the conventional triaxial compression test can be expressed as

$$Q = 3\left[P - \left(P_c - P_p\right)\right] \tag{1}$$

In a conventional compression test, permeability is measured along the axial direction which is parallel to σ_1.

2.2.2. Conventional Triaxial Extension

[19] In a conventional triaxial extension test, the sample is first loaded hydrostatically (i.e., $\sigma_1 = \sigma_2 = \sigma_3$) to a desired hydrostatic pressure P_c, and then while keeping the axial stress ($\sigma_3 = P_c$) constant using a hydraulic ram, the radial stresses ($\sigma_1 = \sigma_2$) are increased using a air-driven pump. The loading path for the conventional triaxial extension test can be described by

$$Q = \frac{3}{2}\left[P - \left(P_c - P_p\right)\right] \tag{2}$$

[20] In a conventional extension test, permeability is measured along the axial direction which is perpendicular to σ_1. Comparison of Equations (1) and (2) shows that the loading paths of a conventional extension and a conventional compression test have at most one coincident stress state in the (P, Q) space (Figure 2), and consequently permeability anisotropy inferred from two such tests has large uncertainties [*Zhu et al.*, 1997].

2.2.3. Hybrid Triaxial Compression

[21] In a hybrid test, after loading the sample hydrostatically to a desired confining pressure P_c, instead of maintaining the radial stresses ($\sigma_3 = \sigma_2$) constant, both the axial stress (σ_1) and radial stresses ($\sigma_3 = \sigma_2$) are increased proportionally using a hydraulic ram and a air driven pump, respectively. By controlling the increment of $\sigma_3 = \sigma_2$ to be 1/4 of that of σ_1, the loading path of such a hybrid test can be expressed as

$$Q = \frac{3}{2}\left[P - \left(P_c - P_p\right)\right] \tag{3}$$

In a hybrid compression test, permeability is measured along the axial direction which is parallel to σ_1. For any conventional extension test, a hybrid compression test can be prescribed with an identical loading path in the (P, Q) space. Therefore the permeability k_1 (parallel to σ_1) measured during the hybrid triaxial compression tests and k_3 (perpendicular to σ_1) obtained during conventional extension tests at identical stress states can be compared to infer permeability anisotropy [*Zhu et al.*, 2002].

2.3. Permeability Data

[22] Laboratory measurements have been conducted on various porous sandstones [*Zhu and Wong*, 1997; *Zhu et al.*, 1997, 2002]. In this paper, we present a subset of the experimental data of Berea sandstone to illustrate the typical

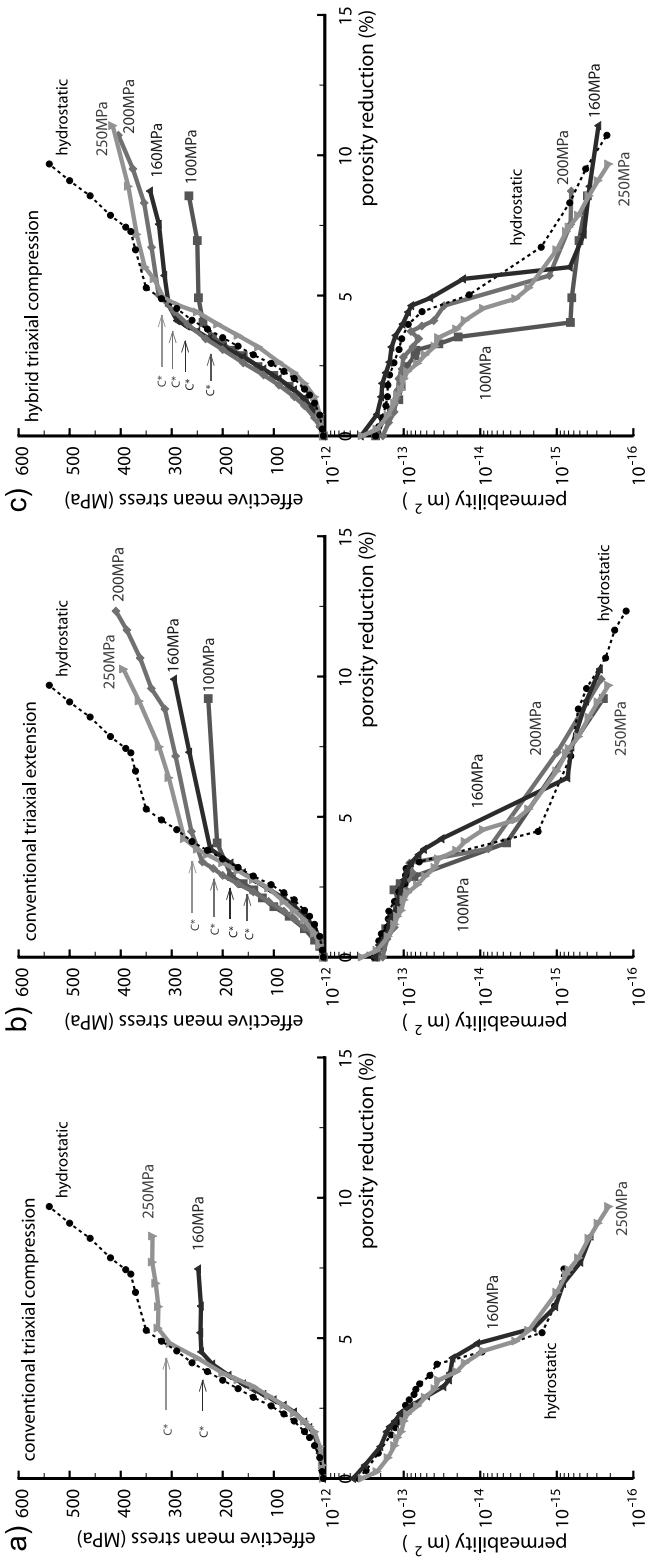

Figure 3. Deformation data and permeability evolution as a function of porosity reduction in (a) Conventional triaxial compression (b) Convential triaxial extension and (c) Hybrid triaxial compression tests. The effective confining pressures are as marked. The compactive yield stress states C^* are indicated by arrows. Note the drastic porosity and permeability reduction that occurred at C^*. For reference, the hydrostatic compression data are shown as dashed curves, where P^* indicates the onset of grain crushing and pore collapse.

behavior of permeability evolution as a function of stress during cataclastic flow.

[23] The Berea sandstone used in these experiments has an initial porosity of 21%. It is composed of 71% quartz, 10% feldspar, 5% carbonate, and 10% clay minerals. Samples are cored perpendicular to their sedimentary bedding, and the samples are 18.4 mm in diameter and 38.1 mm in length. Visual examination of the specimens reveals that the samples are free from macroscopic planar shear features. Tests on intact samples indicate that permeability anisotropy is insignificant before deformation.

[24] The samples were deformed at room temperature with the starting hydrostatic pressure P_c at a value ranging from 110 to 260 MPa, while the pore pressure P_p was fixed at 10 MPa. These confining pressures are sufficiently high to inhibit shear localization [e.g., *Wong et al.*, 1997]. At the beginning of each triaxial test, the initial permeability was measured at P_c = 13 MPa and P_p = 10 MPa (corresponding to an effective pressure of $P_c - P_p$ = 3 MPa which is sufficient to load the jacket tightly around the sample, thus inhibiting leakage along the sample-jacket interface). Permeability was measured along the axial direction during mechanical compaction up to 10% axial strain. Samples retrieved after each test show uniform deformation with neither shear nor compaction localization in the deformed samples. Whole sample thin section analyses under optical microscope also show no discrete localization bands or easily distinguishable compaction localization patches in any of the samples used in this study. Based on these observations, we conclude that the samples are deformed in the cataclastic flow regime.

[25] Figure 3 presents a compilation of the mechanical data (effective mean stress vs. porosity) and the evolution of the permeability-porosity relationship under different loading paths. The effective pressures ($P_c - P_p$) used for each test are indicated in the plot. For reference, the evolution of permeability under hydrostatic loading is also included in Figure 3 as dashed curves. Hydrostatic loading always decreases porosity, with the most significant reduction occurring after the onset of grain crushing and pore collapse at the critical effective pressure P^* [e.g., *Zhang et al.*, 1990; *Wong et al.*, 1997]. During hydrostatic loading, the effective pressure by itself reduces the permeability by more than 3 orders of magnitude [see also *David et al.*, 1994], tracking closely the accelerated porosity reduction beyond P^*.

[26] Comparison of Figures 3a, 3b and 3c clearly shows that the mechanical behavior and permeability evolution are qualitatively similar under different loading paths in the cataclastic flow regime. The application of non-hydrostatic stress leads to "shear-enhanced compaction" [*Wong et al.*, 1997]. When a sample is loaded beyond a compactive yield stress state C^*, considerable deviation of the deformation curves for triaxial tests from the hydrostat can be observed (Figure 3). Permeability evolution closely tracks porosity reduction during compactive loading. There is a positive correlation between permeability and porosity in the cataclastic flow regime. Tabulated data of permeability evolution as functions of stress, axial strain and porosity can be found in *Zhu and Wong* [1997] and *Zhu et al.* [1997, 2002].

[27] Assuming that the permeability tensor and stress tensor have the same principal directions, following the axisymmetry of the sample, *Zhu et al.* [2002] determined the principal components of the permeability tensor by comparing permeability values at identical mean and differential stress states in both extensional and compressional tests. Because the intact samples are free of macroscopic planar shear features and the deformation is homogeneous (pervasive cataclasis), the axisymmetric and coaxial assumptions are justified. Because permeability is always measured along the axial direction, hybrid compression experiments give the evolution of k_1, the permeability along the direction of maximum compression, and conventional extension experiments give k_3, the permeability along the direction of minimum compression. Comparison of experimental data suggested that the maximum principal component of the permeability tensor k_1 generally exceeds the minimum principal component of the permeability tensor k_3 during the development of shear-enhanced compaction. Furthermore, the difference between k_1 and k_3 diminishes when the cumulative axial strain exceeds ~10% [*Zhu et al.*, 2002].

[28] The stress-induced reduction of porosity and permeability in the cataclastic flow regime can be separated into 3 different stages. In Figure 4, we plotted porosity and permeability as functions of differential stress normalized by the stress state at C^*. The distinctive characters of each of the three stages are evident. In stage I, permeability values obtained from hybrid compression and conventional extension tests with identical loading paths are comparable, indicating negligible stress-induced permeability anisotropy. In stage II, our data indicate that k_1 may exceed k_3 by as much as two orders of magnitude [*Zhu et al.*, 2002, Figure 9] in the vicinity of C^*, the reduction of k_1 at C^* is consistently more rapid than that of k_3. Consequently, the anisotropy in permeability becomes less pronounced with the further development of strain hardening and of shear-enhanced compaction in stage III. A transient behavior of the stress-induced permeability anisotropy is observed in these porous lithified rocks.

[29] Based on the experimental data from conventional compression tests, *Zhu and Wong* [1997] proposed a deformation-permeability map as a conceptual model for the coupling of deformation and fluid flow in porous rocks. The data from hybrid compression and conventional extension tests are in good agreement with this conceptual model (Figure 5), indicating that the deformation-permeability relationship is robust under various loading paths. In Figure 5, the compactive yield stresses for the onset of shear-induced dilation in the brittle fracture regime and shear-enhanced compaction in the cataclastic flow regime delineate the boundary of a closed domain in stress space. This boundary also marks the transition from stage I to stage II in terms of the anisotropic development of permeability.

3. Deformation Mechanisms and Microcrack Damage

3.1. 3D Microstructure of Deformed Samples

[30] Laser scanning confocal microscopy (LSCM) provides a non-destructive method to investigate the 3D pore structure of various rocks [*Fredrich et al.*, 1995]. Because most minerals are only weakly fluorescent, *Fredrich et al.*

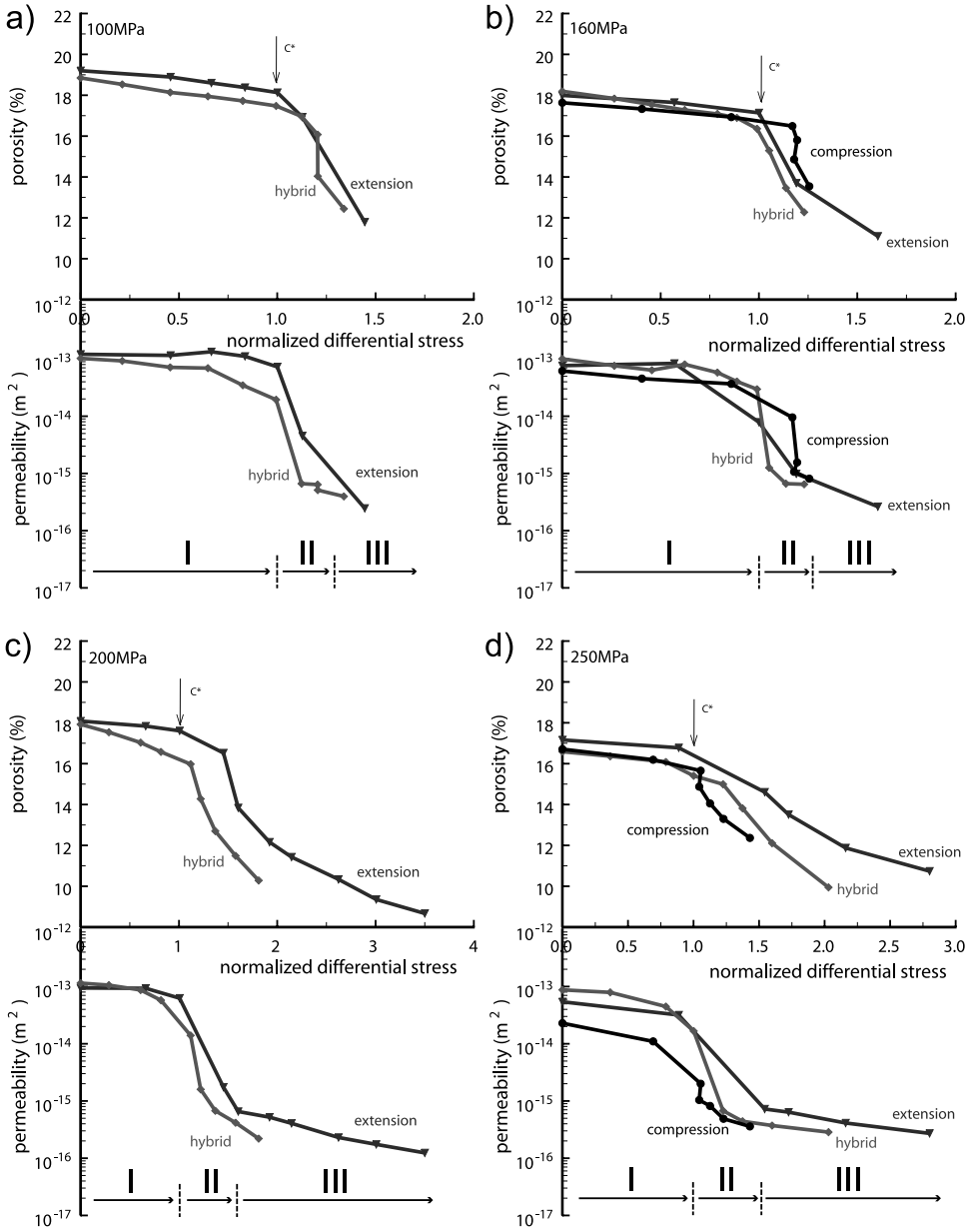

Figure 4. Porosity and permeability as functions of normalized differential stress at effective pressure of (a) 100, (b) 160, (c) 200, and (d) 250 MPa. The compactive yield stress states C^* for the onset of shear-enhanced compaction are indicated by the arrows. Comparison between the data under different loading paths shows that the stress-induced anisotropic permeability reduction in porous rocks can be separated into 3 different stages: before C^* (stage I), at C^* (stage II), and beyond C^* (stage III).

[1995] developed a technique in which a rock sample is impregnated with an ultra-low-viscosity epoxy doped with a fluorochrome to study the void space. A laser beam with suitable wavelength excites the fluorochrome in the epoxy, and the pore structure at the focal plane is illuminated. After collecting a series of successive 2D images at different depths of the sample, a 3D reconstruction can be created using standard image analysis software. Because of its submicron resolution, LCSM provides a useful tool in studying the 3D geometric complexity of the crack distribution in deformed sandstones [*Menéndez et al.*, 2001].

[31] Grain-scale damage in porous sandstones deformed in the cataclastic flow regime consists mainly of intragranular microcracking, grain crushing and pore collapse [*Menéndez et al.*, 1996]. We used a Zeiss LSM-510 system to elucidate the accumulated damage of samples undergone cataclastic failure. A representative 3D reconstruction of the pore space in a deformed sample is shown in Figure 6. The image shows that intragranular microcracks initiate at contact regions where the impingement of grains induces high stress concentration. It also shows that comminuted subparticles of grains collapsed into and filled up the pore space (Figure 6). In general, the 3D pore structure obtained by

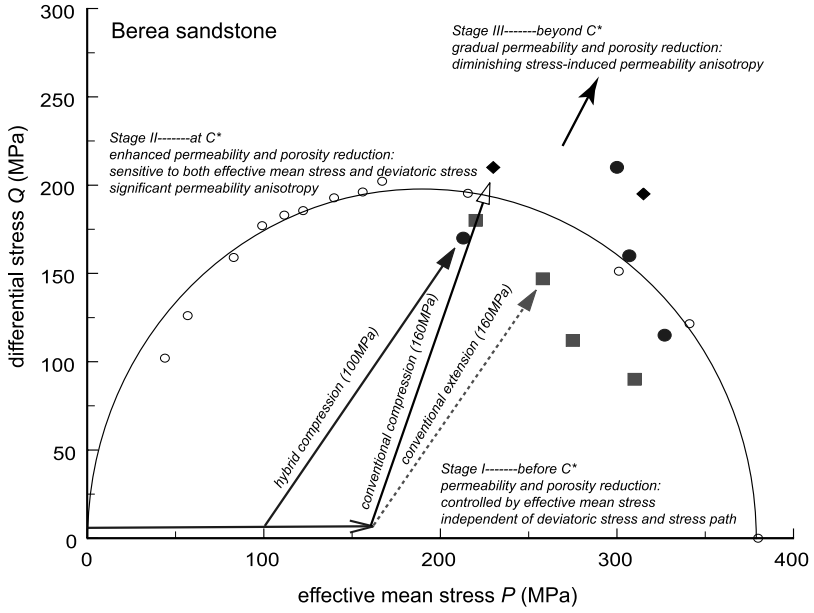

Figure 5. Yield envelope in the (P, Q) stress space for the compactive yield stress C^* of Berea sandstone. Open circles represent data from mechanical tests under conventional compression by *Baud et al.* [2000]. Solid diamonds are data from conventional compression tests [*Zhu and Wong*, 1997]. Solid squares are data from extension tests [*Zhu et al.*, 1997], and solid circles are data from hybrid compression tests [*Zhu et al.*, 2002]. Because of stress corrosion incurred during the "locked" intervals during which permeability values are obtained [*Zhu et al.*, 1997], the yield stresses C^* obtained in permeability tests are generally lower and more scattered than those obtained in continuous mechanical tests [*Wong et al.*, 1997]. The different loading paths are indicated by solid arrows. The yield envelope marks the boundary between the stage I and stage II of stress-induced permeability and porosity reduction.

LCSM is very consistent with the 2D results reported by *Menéndez et al.* [1996] using optical and scanning electron microscopes.

[32] On the basis of the quantitative characterization of damage parameters such as microcrack density and its anisotropy, pore size distribution, and comminuted volume fraction, *Menéndez et al.* [1996] proposed a conceptual micromechanical model for the development of compactive cataclastic flow. In their model, the development of Hertzian fracture is the primary cause for shear-enhanced compaction in the cataclastic flow regime. Below C^*, the relatively low deviatoric stress level induces few intragranular microcracks at grain contacts, and thus the porosity reduction at this stage is similar to that under hydrostatic compaction. At C^*, the intensity of microcracking events increases significantly. Extensive cracking causes pervasive grain comminution and pore collapse, and shear-enhanced compaction is manifest as cracking, which facilitates compaction. Because grain crushing and pore collapse are very efficient in obstructing fluid flow, and stress-induced microcracking is preferentially subparallel to the maximum principal stress, this conceptual model provides a qualitative link between the micromechanical processes and the anisotropic reduction of permeability during compactive cataclastic flow. However, an upscaling relationship is needed to quantify the macroscale anisotropic reduction of permeability caused by microscale damage accumulation in forms of microcracking, grain crushing and pore collapse.

3.2. Acoustic Emission Data

[33] To further understand the deformation processes caused by microcracking, we conducted a few mechanical tests in which the acoustic emission (AE) activity was monitored. A piezoelectric transducer (PZT-7, 5.0 mm diameter, 1 MHz longitudinal resonant frequency) was installed on the flat surface of one of the steel end-plugs attached to the sample. To accommodate the AE transducer, we had to modify the downstream port configuration and thus these tests were conducted without permeability measurements. Therefore the loading was continuous in these tests at a strain rate of 2.6×10^{-5}/s. The AE signals were conditioned by a preamplifier (gain 40dB, frequency response 1.5 kHz to 5 MHz) that distinguishes AE events from electric spikes. More technical details are presented by *Zhang et al.* [1990].

[34] In Figure 7, we plot the change in AE rate during cataclastic flow for Berea sandstone samples deformed at effective pressure of 200 MPa under conventional compression. Our data clearly shown that before C^*, the AE rate stays relatively constant. The onset of shear-enhanced compaction C^* is marked by a surge in AE activity, where a sudden increase in AE rate was observed (Figure 7a). Notice that when loaded beyond C^*, the AE rate peaks and then levels off (Figure 7a). The same AE data are plotted as a function of the effective mean stress in Figure 7b. Interestingly, the change in AE rate forms a bell-shaped curve around its peak (Figure 7b). Because AE activity is

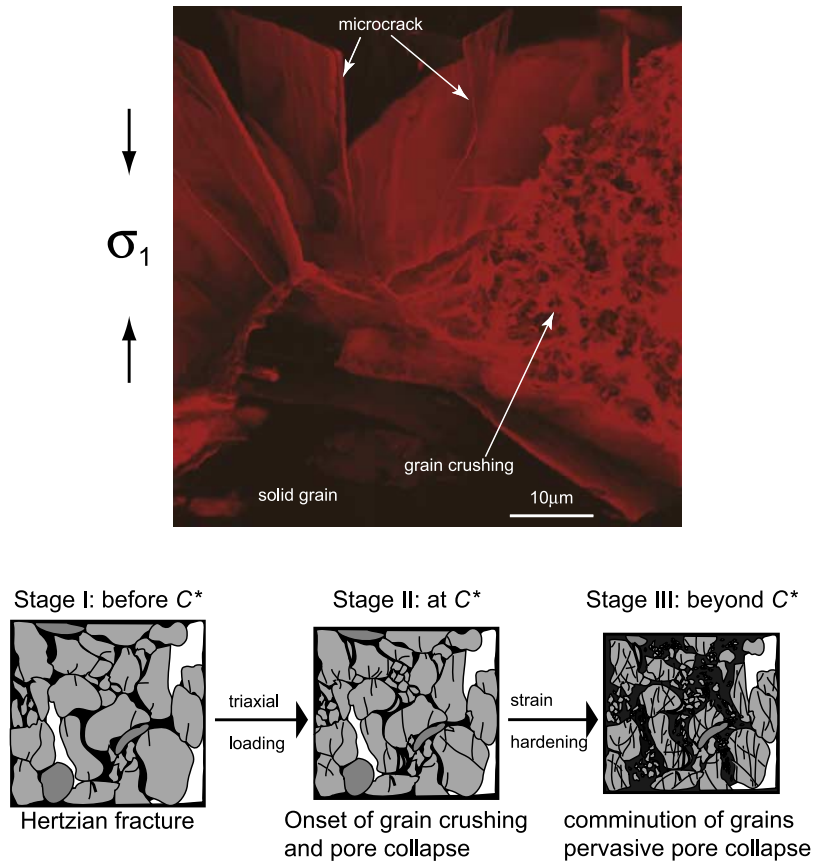

Figure 6. The upper panel shows a 3-D laser confocal micrograph of a Berea sandstone samples at 200 MPa. The lighter regions are voids. The orientation of maximum principal stress σ_1 is indicated. Following *Menéndez et al.* [1996], the key microstructural features at three different stages—Before, at, and beyond C^* are summarized in the lower panel.

associated with fracturing events occurring during deformation [e.g., *Lockner et al.*, 1992], the AE rate reflects the intensity of microcrack damage processes.

4. A Probabilistic Damage Model

[35] Compaction-induced permeability reduction under hydrostatic loading can be approximated before P^* by an exponential function [*David et al.*, 1994]:

$$k^H/k_{ref} = \exp\left[\gamma\left(P_{eff} - P_{ref}\right)\right] \quad or \quad \ln\left(k^H\right) = \ln\left(k_{ref}\right) - \gamma\left(P_{eff} - P_{ref}\right) \tag{4}$$

where k^H is the permeability at the effective pressure P_{eff}, and k_{ref} is the permeability at a reference effective pressure P_{ref}, and γ is the pressure sensitivity coefficient that depends on rock type.

[36] The exponential law can be readily adopted to represent the effect of effective mean stress on permeability evolution during cataclastic flow. Indeed, *Zhu* [2006] demonstrates that the exponential law provides a very good approximation to the relation between permeability and effective mean stress before C^*. As pore size reduction caused by isostatic compaction doesn't show observable anisotropy, no permeability anisotropy is expected in stage I, as is observed indeed (Figure 4). Thus the measured permeability reduction follows the exponential law (4) in stage I.

[37] The exponential law alone cannot capture the drastic permeability reduction and permeability anisotropy observed in stages II and III. It is necessary to develop a model taking the effect of deviatoric stress into account. Motivated by the microstructural observations and AE data, *Zhu* [2006] proposed a probabilistic damage model that quantifies the permeability reduction during shear-enhanced compaction. This model is based on the following micromechanical concepts: 1) Hertzian fracture occurs when the local stress acting at a grain contact exceeds a certain threshold; 2) Cracking-induced grain crushing and pore collapse are the main causes responsible for the significant permeability reduction associated with compactive cataclastic flow. Using the probabilistic damage model, *Zhu* [2006] successfully reproduces the drastic permeability reduction at C^*. In this study, we will extend the probabilistic model to characterize the stress-induced permeability anisotropy during cataclastic flow.

4.1. Characterization of Cumulative Damage

[38] When subjected to loading, the local stresses at grain contacts in a polymineralic rock are heterogeneous. Below C^*, due to low stress levels, only a few grain contacts experience local stresses above the Hertzian fracture thresh-

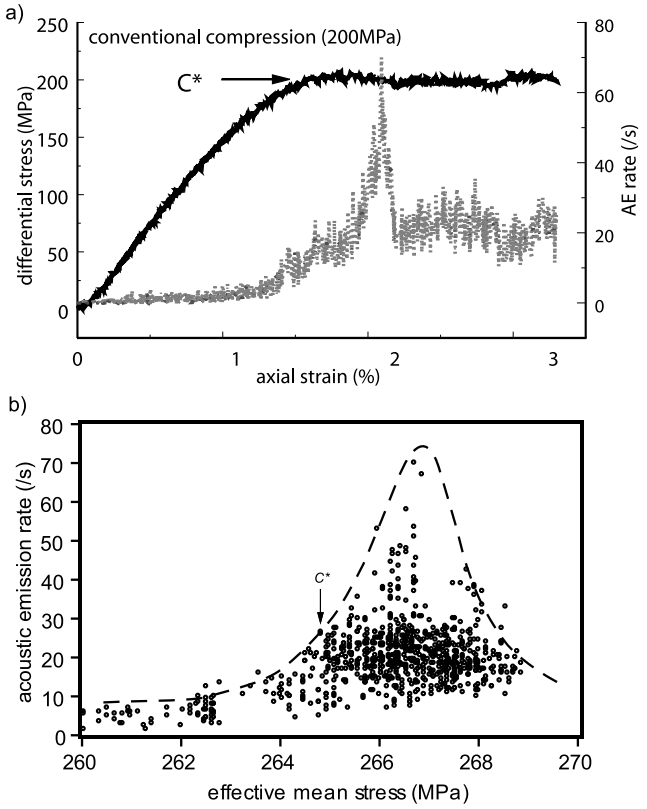

Figure 7. (a) Differential stress and acoustic emission (AE) rate as functions of axial strain for a conventional compression test at effective pressure of 200 MPa. In this test, the loading was continuous and AE activity during deformation was monitored. (b) Same AE data as a function of the effective mean stress at the vicinity of C^*. Notice that a Gaussian function (dashed curve) can be used to approximate the AE activity distribution as a function of effective mean stress The compactive yield stress states C^*, which is marked by a surge in AE activity, are indicated by the arrows. Note that AE activity peaks after C^* and levels off at larger strain.

old. Hence only sparse cracking events occur. When the sample is loaded beyond C^*, however, the local stresses at majority of the grain contacts exceed the threshold, resulting in extensive microcracking. Without better laboratory constraints, we choose a normal (Gaussian) distribution to represent the probability density function of damage in the form of microcracking under non-hydrostatic stress:

$$f(\sigma) = \frac{1}{\sqrt{2\pi}\delta} e^{-\frac{(\sigma-\mu)^2}{2\delta^2}} \tag{5}$$

where σ is the applied stress, μ and δ are the mean and standard deviation of the Gaussian distribution, respectively (Figure 8). For a given axisymmetric loading path, there is a one-to-one correspondence between the effective mean stress P and differential stress Q. Here we use P as the independent stress variable, σ, but it should be noted that most of the results derived here can alternatively be expressed in terms of Q. In our model, δ represents the grain scale heterogeneity in local stress concentration, and can be obtained from the experimental data as one half of the effective stress range over which drastic permeability and porosity reduction occur. The coefficient μ corresponds to the effective mean stress at which the intensity of damage caused by nonhydrostatic stress reaches its maximum. As indicated in Figure 8 this stress level is somewhat higher than that at the onset of shear-enhanced compaction C^*, i.e., $C^* \sim \mu - \delta$. If AE activity is representative of the damage process, then Figure 7b shows that the choice of a Gaussian distribution is reasonable.

[39] The cumulative damage during shear-enhanced compaction can be quantified by a cumulative distribution function:

$$\Phi(P) = \frac{1}{\sqrt{2\pi}\delta} \int_{-\infty}^{P} e^{-\frac{(\sigma-\mu)^2}{2\delta^2}} d\sigma \tag{6}$$

where P is the applied effective mean stress. Although the mathematical definition here specifies the lower limit of integration to be at $\sigma = -\infty$, for practical applications we can choose the lower limit to be at a positive value P_0 on the loading path before the application of differential stress. In particular we choose $P_0 = P_{ref}$ during the initial hydrostatic loading selected in (4). Schematic illustrations of the probability density function and cumulative distribution function are presented in Figure 8.

[40] As shown in Figure 8, this model captures the 3-stage development of stress-induced damage during cataclastic flow. Before C^*, P is much less than μ, and damage caused by the non-hydrostatic stress is negligible. This corresponds to stage I, where microcracks are sparse and the AE activity is low. C^* marks the critical point beyond which $-\delta \leq P - \mu \leq \delta$, where fracturing occurs at the majority of the grain contacts (say, 95th percentile in the Gaussian distribution, Figure 8). This agrees well with the surge in AE activity and the increase in microcrack density in stage II. According to our model, when loaded further beyond C^*, where $P - \mu \gg \delta$, the fracturing activity levels off (stage III).

[41] Assuming that the damage process can be modeled as the accumulation of a number of discrete events, each of which produces identical local permeability reduction, and that the macroscopic permeability reduction is given by the geometrical mean of the local permeability reduction induced by these discrete events [*Madden*, 1976], the overall permeability reduction induced by deviatoric stress can be expressed as:

$$\ln k^D = \beta \Phi(P) \tag{8a}$$

where β is a proportionality coefficient. Introducing a new variable $s = (\sigma - \mu)/\delta$ and rearranging expression (8a), we have

$$\ln(k^D) = \beta \frac{1}{\sqrt{2\pi}} \int_{-\infty}^{\frac{P-\mu}{\delta}} e^{-\frac{s^2}{2}} ds$$

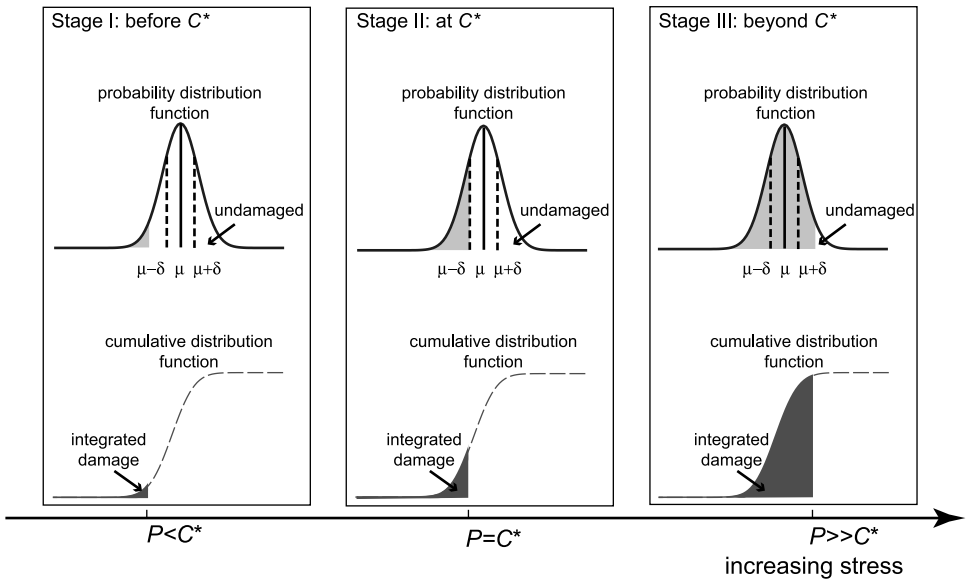

Figure 8. Schematic representation of the probabilistic damage model. A Gaussian distribution is chosen as probability density function of damage under a given stress (bell curve). The cumulative damage function is shown as the dashed curve. In stage I, the effective mean stress P is much less than the mean of the Gaussian distribution μ, so only a few Hertzian fractures occur, leaving the majority of the grains intact (shaded area inside the bell curve) and the cumulative damage negligible (shaded area under the dashed line). Most of the damage occurs during stage II, when $\mu - \delta \le P \le \mu + \delta$, which results in drastic increase in cumulative damage. In stage III, $P \gg \mu$, extensive grain comminution is observed, whereas further increase in stress results in little additional damage.

i.e.,

$$\ln(k^D) = \beta\frac{1}{\sqrt{2\pi}}\left[\int_{-\infty}^{0} e^{-\frac{s^2}{2}}ds - \int_{0}^{\frac{\mu-P}{\delta}} e^{-\frac{s^2}{2}}ds\right] = \frac{\beta}{2}\left[\left(1 - \mathrm{erf}\left(\frac{\mu-P}{\delta}\right)\right]\right. \quad when\ P < \mu$$

$$\ln(k^D) = \beta\frac{1}{\sqrt{2\pi}}\left[\int_{-\infty}^{0} e^{-\frac{s^2}{2}}ds + \int_{0}^{\frac{P-\mu}{\delta}} e^{-\frac{s^2}{2}}ds\right] = \frac{\beta}{2}\left[\left(1 + \mathrm{erf}\left(\frac{P-\mu}{\delta}\right)\right]\right. \quad when\ P \ge \mu \tag{8b}$$

With the error function defined as:

$$\mathrm{erf}(x) = \frac{2}{\sqrt{\pi}}\int_0^x e^{-t^2}dt, \quad x \ge 0$$

Expression (8b) quantifies the permeability loss due to the application of deviatoric stress in the cataclastic flow regime. Combining expression (4) and (8b), we obtain a unified expression for permeability in the cataclastic flow regime:

$$\ln k = \ln(k^H) - \ln(k^D) = \ln(k_{ref}) - \gamma(P_{ref} - P) - \frac{\beta}{2}\left[1 + \mathrm{sign}(P-\mu)\mathrm{erf}\left(\left|\frac{P-\mu}{\delta}\right|\right)\right] \tag{9a}$$

or

$$\ln k = A - \gamma P - \mathrm{sign}(P-\mu)\frac{\beta}{2}\mathrm{erf}\left(\left|\frac{P-\mu}{\delta}\right|\right) \tag{9b}$$

where

$$A = \ln k_{ref} + \gamma P_{ref} - \frac{\beta}{2}$$

Expressions (9a) and (9b) take the minus sign before the error function when $P < \mu$, and plus sign when $P \ge \mu$.

[42] As clearly shown in expression (9b), the influences of the effective mean stress and deviatoric stress on permeability can be accounted for in separated terms in our model. While the second term $-\gamma P$ quantifies the effective mean stress influence, the deviatoric stress effect is quantified by the last term with the error function. When the effective mean stress P is below the critical yield stress C^* (i.e., $P \ll \mu$), erf$[|P - \mu|/\delta]$ is very small (Figure 8). Therefore the deviatoric stress term in expression (9) is negligible and the effective mean stress exerts the dominant control over permeability reduction in stage I. When the effective mean stress P is in the vicinity of C^*, erf$[|P - \mu|/\delta]$ changes very rapidly (Figure 8), and expression (9) is dominated by the deviatoric stress term. This corresponds to stage II, in which drastic permeability reduction occurs. Because different coefficients μ and δ in the error function are observed in the extension and compression tests, this cumulative dam-

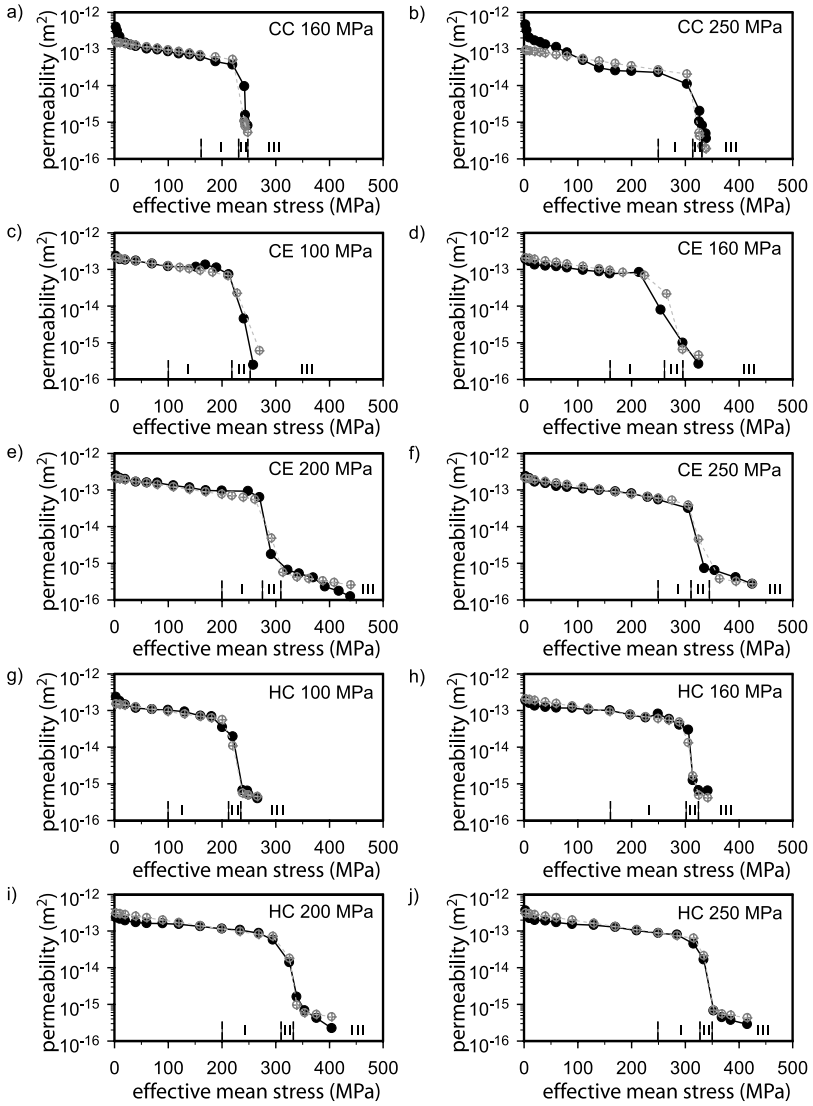

Figure 9. Comparison of the modeling results (open symbols with crosses) to the experimental data (solid symbols) of Berea sandstone for conventional compression (CC) at effective pressure of (a) 160 and (b) 250 MPa; conventional extension (CE) at (c) 100, (d) 160, (e) 200, and (f) 250 MPa; hybrid compression (HC) at (g) 100, (h) 160, (i) 200, and (j) 250 MPa. The 3 different stages are separated by the dashed lines. The onset of shear-enhanced compaction C^* corresponds to the transition from stage I to stage II.

age model provides a quantitative measure of development of anisotropic permeability. The calculated permeability values are compared to the experimental data in Figure 9. The good agreement between the two indicates that the probabilistic damage model provides an appropriate quantitative tool to characterize the anisotropic reduction of permeability during shear-enhanced compaction. Fitting values for coefficients γ, β, μ and δ are compiled in Table 1.

4.2. Anisotropic Development of Permeability With Stress

[43] Our probabilistic damage model has been derived on the basis of the mechanical behavior and permeability evolution of Berea sandstone, for which the most comprehensive data set exists. To validate our model, we apply expression (9) to data collected for other porous sandstones. The evolution of permeability and its anisotropy was measured in both Adamswiller and Rothbach sandstones following the experimental methodology described above [*Zhu et al.*, 2002]. Adamswiller and Rothbach sandstones have initial porosities of 23% and 20%, respectively. Detailed petrophysical descriptions of these two sandstones were presented in *Wong et al.* [1997]. The model predictions of permeability are compared to the experimental data in Figure 10. The values for the coefficients γ, β, μ and δ used in the simulations are given in Table 2.

[44] The stress state μ at the peak of the Gaussian distribution (Figure 8) marks the critical stress state at which the damage rate is maximum. The values of permeability at this critical stress mark the midpoint of the total

Table 1. Simulation Parameters for Berea Sandstone

		Berea Sandstone (21%)				
P_0 (MPa)	C^*(MPa)	γ (MPa^{-1})	β	μ (MPa)	δ (MPa)	k_{ref} (at P_{ref} = 0) (m^2)
				Conventional Compression		
160[a]	230	0.005	4.5	237	7	1.5×10^{-13}
250[b]	315	0.005	4.5	322	7	9.4×10^{-14}
				Conventional Extension		
100[b]	220	0.005	4.5	237	17	1.5×10^{-13}
160[b]	258	0.005	4.5	275	17	1.5×10^{-13}
200[b]	275	0.005	4.5	292	17	1.5×10^{-13}
250[b]	310	0.005	4.5	327	17	1.5×10^{-13}
				Hybrid Compression		
100[c]	213	0.005	4.5	223	10	1.5×10^{-13}
160[c]	300	0.005	4.5	310	10	1.5×10^{-13}
200[c]	307	0.005	4.5	317	10	3.1×10^{-13}
250[c]	327	0.005	4.5	337	10	3.1×10^{-13}

[a]Detailed mechanical and permeability data can be found in *Zhu and Wong* [1997].
[b]Detailed mechanical and permeability data can be found in *Zhu et al.* [1997].
[c]Detailed mechanical and permeability data can be found in *Zhu et al.* [2002].

permeability reduction associated with the shear-enhanced compaction.

$$\ln k_\mu = A - \gamma\mu \tag{10}$$

[45] The determination of the critical stress state C^* is not very well constrained in permeability experiments. There are two reasons for the large uncertainties in C^*. First, stress relaxation occurs in permeability experiments, because deformation is stopped during the permeability measurement steps, during which hydraulic ram is locked. Second, AE data, which provide less ambiguous indication of C^* than porosity data alone, cannot be collected due to lack of space in the sample column [e.g., *Zhu et al.*, 1997], Therefore μ values carry relatively large uncertainties. By comparison, the δ values are more precise and more consistent, as 2δ correspond to the clearly defined range of effective mean stress during which drastic stress-induced permeability reduction occurs. Combining C^* values obtained from the mechanical tests (with AE data and continuous deformation, see *Wong et al.* [1997]) and δ obtained from permeability tests, we observe that

$$\mu = C^* + \delta \tag{11}$$

[46] In Figure 11 we plotted the stress state μ for all three sandstones. The stress state μ follows approximately an elliptical cap in P-Q space that depends on rock type, analogous to that of the compactive yield stress C^* in porous rocks [*Wong et al.*, 1997]. This reflects the small variability of the parameter δ on stress conditions for a given sandstone and loading configuration. Because the first and second invariants of the stress tensor control the deformation of a porous rock, elliptical caps C^* are identical in the hybrid compression tests and the conventional extension texts (Figure 5). However, the differences in δ (grain-scale stress variation sensitive to loading history) are reflected in the elliptical caps of the maximum damage rate stress μ (Figure 11). The differences in the elliptical caps of stress μ (Figure 11) provide a quantitative measure of stress-induced permeability anisotropy during shear-enhanced compaction.

[47] We fitted our data for μ to the ellipse (Figure 11)

$$\frac{(P-c)^2}{a^2} + \frac{Q^2}{b^2} = 1 \tag{12}$$

where a and b are the semi-axes and c is the center of the ellipse. The tabulated parameters a, b and c can be found in Table 3.

[48] The loading paths we used are given by

$$Q = \frac{P - (P_c - P_p)}{\alpha} \tag{13}$$

with α = 2/3 for conventional triaxial extension and hybrid compression tests and α = 1/3 for conventional triaxial compression tests. Substituting (13) into (12) and solving for the value of P that falls on the ellipse mapped out by the data in Figure 11, we obtain

$$\mu = \frac{\left[a^2(P_c - P_p) + \alpha^2 b^2 c\right] + \alpha a b\sqrt{\left[a^2 + \alpha^2 b^2\right] - \left[c - (P_c - P_p)\right]^2}}{(a^2 + \alpha^2 b^2)} \tag{14}$$

This allows us to identify the value of μ that can be substituted into Equation (9) to calculate the permeability once the heterogeneity coefficient δ has been specified.

[49] Using Equation (14), the evolution of permeability can be mapped out in the stress space as contours of permeability or normalized permeability by the value $k\mu$ at $P = \mu$ on the ellipse. The predicted iso-permeability contours of Berea sandstone using 3 different loading configurations are shown in Figure 12.

5. Discussion

[50] We presented a unified model to quantify the effects of stress on the anisotropic reduction of permeability during

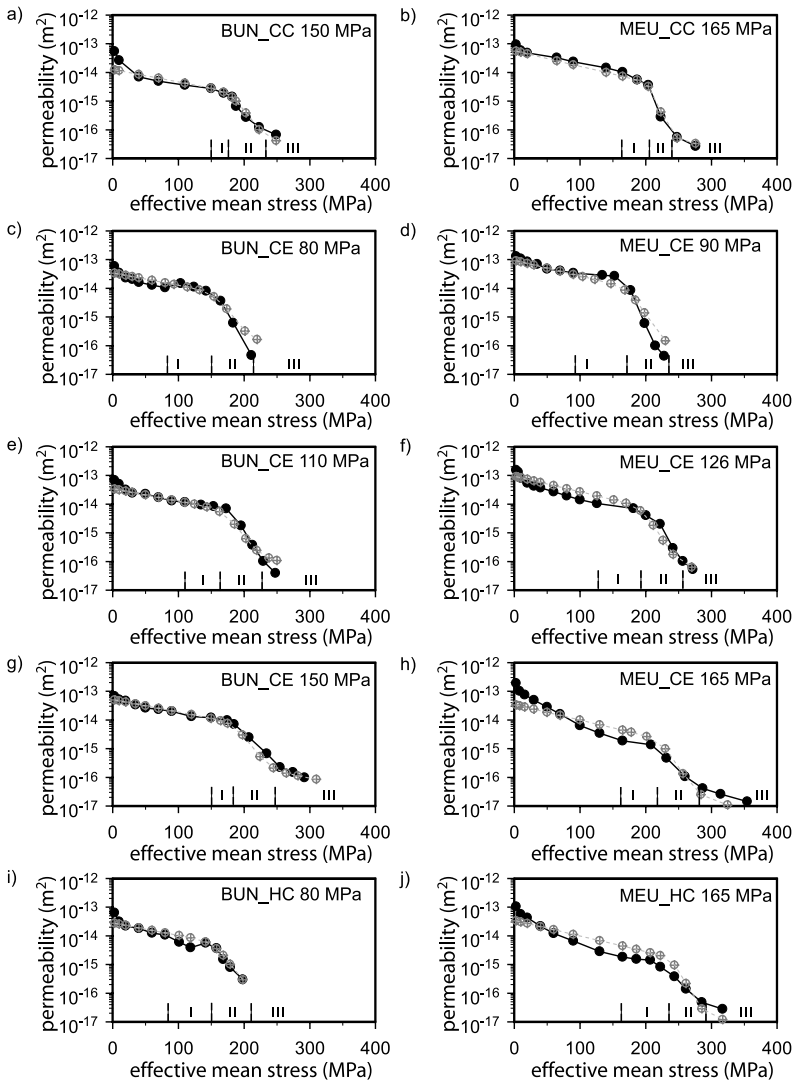

Figure 10. Comparison of the modeling results (open symbols with crosses) to the experimental data (solid symbols) of Adamswiller (BUN) and Rothbach (MEU) sandstones, respectively, for conventional compression (CC) at effective pressure of (a) 160 and (b) 165 MPa; conventional extension (CE) at (c) 80, (d) 90, (e) 110, (f) 126, (g) 150, (h) 165 MPa; hybrid compression (HC) at (i) 80, and (j) 165 MPa. The three different stages are separated by the dashed lines. The onset of shear-enhanced compaction C^* corresponds to the transition from stage I to stage II.

cataclastic flow. In our model, the exponential law proposed by *David et al.* [1994] is adopted to link permeability reduction to effective mean stress. An additional permeability reduction caused by the application of deviatoric stress is calculated using a probabilistic damage model, which is derived on the basis of microstructural observations. Because the microscale damage consists primarily of microcracking and microcracking-facilitated grain crushing and pore collapse, our model is consistent with the observation that the transition from stage I to stage II marks the transition from pore-controlled permeability to crack-controlled permeability [*Fortin et al.*, 2005]. Without systematic data on the evolution of crack density and crack aperture of samples deformed under various loading paths, we made the assumption that the development of grain-scale damage follows a Gaussian distribution. Our probabilistic damage model captures the drastic change in permeability anisotropy before and after the onset of shear-enhanced compaction. The four fitting parameters involved in this model, γ, β, μ and δ, discussed below, can be extracted from laboratory measurements.

5.1. Effective Mean Stress Sensitivity Coefficient γ

[51] *Menéndez et al.* [1996] show that the porosity of intact Berea sandstone is constituted primarily of well-connected equant and tubular pores, with very little pre-existing anisotropy. Increasing the effective mean stress reduces the average pore size, without evident anisotropy in pore size distribution during mechanical compaction [*Menéndez et al.*, 1996]. Accordingly, experimental measurements show that permeability reduction before shear-enhanced compaction, when the effective mean stress exerts the dominant control, has very little anisotropy. Therefore while the effective mean stress sensitivity coefficient γ is

Table 2. Simulation Parameters for Adamswiller and Rothbach Sandstones

P_0, MPa	C^*, MPa	γ, MPa^{-1}	β	μ, MPa	δ, MPa	k_{ref} (at $P_{ref}=0$) (m^2)
Adamswiller Sandstone (22.6%)						
Conventional Compression						
150[a]	176	0.01	3.3	206	30	1.3×10^{-14}
Conventional Extension						
80[b]	150	0.01	3.3	182	32	3.4×10^{-14}
110[b]	165	0.01	3.3	197	32	3.4×10^{-14}
150[b]	180	0.01	3.3	212	32	5.1×10^{-14}
Hybrid Compression						
80[c]	150	0.01	3.3	181	31	2.8×10^{-14}
Rothbach Sandstone (19.9%)						
Conventional Compression						
165[a]	204	0.0125	4	222	18	5.7×10^{-14}
Conventional Extension						
90[b]	170	0.0125	4	202	32	9.4×10^{-14}
126[b]	190	0.0125	4	222	32	9.4×10^{-13}
165[b]	220	0.0125	4	252	32	3.4×10^{-13}
Hybrid Compression						
165[c]	238	0.0125	4	264	26	3.4×10^{-14}

[a]Detailed mechanical and permeability data can be found in *Zhu and Wong* [1997].
[b]Detailed mechanical and permeability data can be found in *Zhu et al.* [1997].
[c]Detailed mechanical and permeability data can be found in *Zhu et al.* [2002].

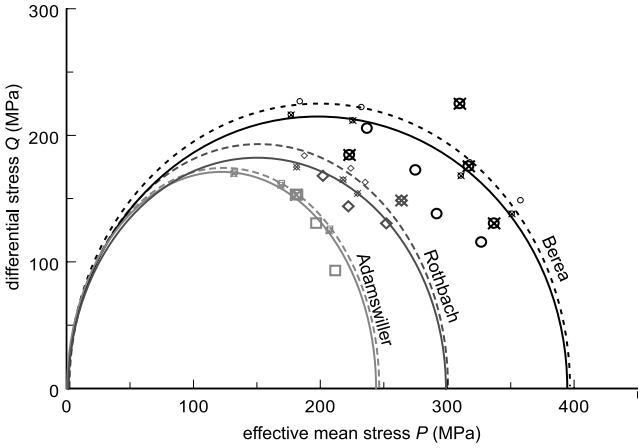

Figure 11. Elliptical envelopes of maximum damage rate stress μ in *P-Q* space for Adamswiller (grey), Berea (black), Rothbach (dark grey) sandstones. Solid curves are elliptical caps during hybrid compression loading. Dashed curves are elliptical caps during extension loading. The difference between the solid curve and dashed curve represents the anisotropic development of permeability during shear-enhanced compaction. Values of μ extracted from our permeability measurements are plotted as well, with open symbols (squares—Adamswiller, diamonds—Rothbach, and circles—Berea) representing data from extension tests, and symbols with crosses representing data from hybrid tests. The larger symbols represent values obtained in permeability tests, the smaller symbols are data inferred from the mechanical tests in *Wong et al.* [1997].

most likely different for different type of rocks [see *David et al.*, 1994; *Wong and Zhu*, 1999], it should be independent of loading paths and effective pressure. Indeed, we found that a single value of 0.5×10^{-2} MPa^{-1} could lead to satisfactory simulation results for all of the experimental data on Berea sandstone under various loading paths (Figure 9) while higher values are appropriate for the other sandstones (Table 2).

5.2. Coefficient β

[52] One important experimental observation is the decoupling of the influences of effective mean stress and deviatoric stress on porosity and permeability during shear-enhanced compaction. The application of a deviatoric stress facilitates drastic porosity removal by inducing microcracks that lead to grain crushing and pore collapse. The proportionality coefficient β is introduced in our model to account for the magnitude of total permeability reduction during the shear-enhanced compaction. Experimental data suggest the total permeability drop during cataclastic flow is approximately constant regardless of loading path and effective pressure [*Zhu et al.*, 1997, 2002]. While this observation

Table 3. Simulation Parameters for Elliptical Caps of μ in *P-Q* Space

		Conventional Compression			Conventional Extension			Hybrid Compression		
P_0, MPa	C^*, MPa	a, MPa	b, MPa	c, MPa	a, MPa	b, MPa	c, MPa	a, MPa	b, MPa	c, MPa
Adamswiller			δ = 30, MPa			δ = 32, MPa			δ = 31, MPa	
60	101	123	215	123	123	175	123	123	172	123
100	138									
150	176									
Berea			δ = 7, MPa			δ = 17, MPa			δ = 10, MPa	
100	167	196	220	196	196	228	196	196	215	196
150	216									
250	301									
300	341									
Rothbach			δ = 18, MPa			δ = 32, MPa			δ = 26, MPa	
110	155	150	192	150	150	196	150	150	188	150
150	192									
165	203									

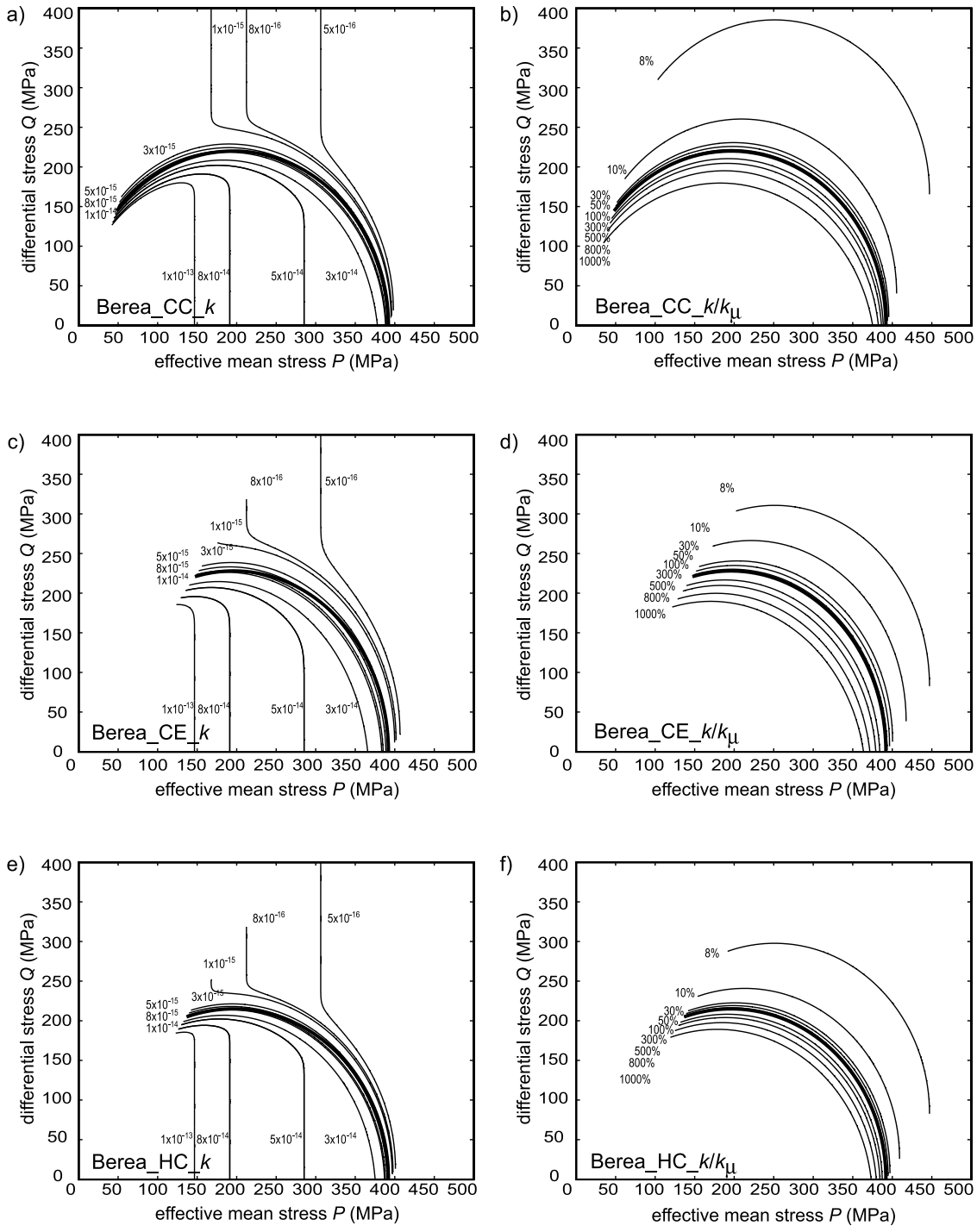

Figure 12. Predicted permeability evolution of Berea sandstone during compactive cataclastic flow. Contours of permeability values (left column) and permeability normalized to its value at μ (right column) for Berea sandstone are plotted for conventional compression (CC) loading configuration: (a) and (b); conventional extension (CE): (c) and (d); and hybrid compression (HC): (e) and (f).

may have some important implications on the damage processes during shear-enhanced compaction, the current experimental data are not precise enough to draw any definite conclusion. To simplify the simulation, a constant β value is chosen in this study (Tables 1 and 2).

5.3. Coefficients μ and δ for Gaussian Distribution

[53] Microstructural observations show that Hertzian fracturing initiated at grain contacts is the dominant micromechanical process during compactive cataclastic flow [*Gallagher et al.*, 1974; *Menéndez et al.*, 1996]. Because of grain-scale stress heterogeneity, damage in the form of

Hertzian fractures occurs over a range of external loading stress. To simplify the analysis without losing generality, we chose the probability distribution function for damage to be Gaussian. It is interesting to notice that the coefficient μ of the Gaussian distribution corresponds to the effective mean stress at which AE rate reaches its maximum (Figure 7). This observation is consistent with the notion that the damage rate reaches its maximum intensity at μ (i.e., peak of the Gaussian distribution). The standard deviation δ can be obtained from the difference in the effective mean stress for the surge of AE (i.e., C^*) and the maximum AE rate (Figure 7), providing an independent constraint on the coefficients μ and δ for the Gaussian distribution. Unfortunately, we could not measure AE activity during permeability tests due to the lack of space for AE transducers in the sample column setup. Instead, we have to pick these coefficients separately from the porosity and permeability data, which inevitably introduces larger uncertainties. In our simulation, δ is chosen to be one half of the stress range over which significant permeability reduction occurs, and μ is defined as the stress level that marks the midpoint of the significant permeability reduction (Figure 4). Notwithstanding some uncertainties in choosing μ and δ, there is a general good agreement between our simulation results and experimental data (Figure 9).

5.4. Stress-Induced Permeability Anisotropy

[54] Significant anisotropy in microcrack density was observed in samples subjected to shear-enhanced compaction [*Menéndez et al.*, 1996]. Stress-induced microcracking develops preferentially sub-parallel to the maximum principal stress σ_1. Whereas the overall decrease in pore size due to pore collapse is responsible for the drastic decrease of permeability associated with the development of shear-enhanced compaction, the anisotropy of microcrack induces permeability anisotropy in the vicinity of the compactive yield stress C^*. Recent laboratory data for hybrid compression [*Zhu et al.*, 2002] and conventional extension tests [*Zhu et al.*, 1997] are for identical loading paths but with flow along two orthogonal directions. When these two sets of data are compared, the permeability for flow parallel to the maximum compression direction is generally greater than perpendicular ($k_1 > k_3$). Using the probabilistic damage model, differences in permeability evolution under various stress paths can be quantified as variations in the parameters δ and μ of the cumulative damage distribution function. The coefficient δ appears larger in extension tests, describing the faster decrease of the permeability along the minimum compression direction and development of permeability anisotropy at C^*.

[55] *Wong et al.* [1997] proposed that the compactive yield stress C^* for porous rocks maps out an elliptical yield envelope in the (P, Q) stress space, in accordance with the critical stress state [*Schofield and Wroth*, 1968] and cap [*DiMaggio and Sandler*, 1971] models. Such an elliptical yield envelope fits our experimental data reasonably well for various loading paths (Figure 5). There is a considerable discrepancy between the cap defined by values of C^* obtained from mechanical tests alone (open circles in Figure 5) and those C^*s obtained from various permeability tests (solid symbols in Figure 5). Some of the scattering can be explained by the lack of AE activity monitoring in these permeability tests—to determine C^* using only porosity data obviously introduces large uncertainty (see Figure 3). In addition, the scattering is aggravated by stress relaxation during the "locked" periods of permeability measurements because the magnitude of stress corrosion varies in different experiments conducted at different effective pressures.

[56] Given these uncertainties, it is difficult to resolve whether different yield envelopes would provide better fits to yield stresses obtained under different loading paths [*Grueschow and Rudnicki*, 2005; *Fortin et al.*, 2006]. However, *Zhu et al.* [2002] conducted mechanical tests on Berea sandstone using both conventional extension and hybrid compression loading configurations. Without stress corrosion and with the help of AE data, they found that C^* values obtained in both the extension and hybrid tests agree remarkably well with those obtained under conventional compression [*Zhu et al.*, 2002, Figure 8a]. This leads us to conclude that, to a first order approximation, C^* is a function of only the first and second stress invariants, which correspond to P and Q respectively in an axi-symmetrical configuration. Nevertheless, more experimental data using non-conventional loading paths are needed to understand the effect of intermediate stress on the yield envelope.

[57] Whereas C^* is stress path-independent, the development of pervasive anisotropic microcracking beyond C^* is apparently sensitive to loading configuration. It is important to realize that even though there is large uncertainty in C^*, the stress range over which significant permeability reduction occurs (i.e., 2δ) is robust. As shown in Figure 4, the slope of permeability versus stress in a hybrid compression test is consistently steeper than that in a corresponding extension test. This phenomenon can not be explained by simply shifting C^*. Through expression (9), our model provides a quantitative measure of how stresses induce the permeability components to evolve at somewhat different rates at different orientations. We find that the stress range over which permeability decreases, 2δ, is systematically larger in extension tests, when k_3 is measured.

5.5. Compaction Localization

[58] Recent studies showed that compaction localization occurs in some porous sandstones with stress states in the transitional regime between brittle faulting and homogeneous cataclastic flow [e.g., *Baud et al.*, 2006]. Visual examination of our deformed samples revealed no discrete compaction band. Examination of whole sample thin sections under optical microscope further indicates no compaction localization patch. *Baud et al.* [2006] observed diffuse compaction bands in Berea sandstone samples deformed at effective pressures between 100 to 150MPa (i.e., transitional regime), and homogeneous cataclastic flow in samples deformed at and above a effective pressure of 200MPa using conventional compression loading path [*Baud et al.*, 2006]. As illustrated in Figure 5, a sample deformed under a effective pressure of 100MPa in the extension or hybrid compression tests reaches roughly the same stress state on the failure envelope as a sample deformed with a effective pressure of 160MPa under conventional compression. Because the effective pressures used in this study are 100, 160, 200, and 250MPa (see Table 1), it is reasonable to conclude that most of the Berea sandstone samples are deformed in the homogeneous cata-

clastic flow regime although weak diffuse compaction bands may occur in samples deformed at the lowest effective pressures, i.e., 160MPa in conventional compression test and 100 MPa in non-conventional tests. Because of the qualitatively similar hydromechanical behavior between these samples and the ones failed by homogeneous cataclastic flow, it is not necessary to consider explicitly compaction localization in our model to simulate the anisotropic reduction of permeability associated with shear-enhanced compaction.

[59] The mechanical behavior of Rothbach sandstone is similar to that of Berea sandstone in that diffuse compaction localization occurs in the transitional regime [e.g., *Bésuelle*, 2001]. In Adamswiller sandstone, however, *Baud et al.* [2006] concluded that homogeneous cataclastic flow is the dominant failure mode. Granted, whether the microscale damage is considered homogeneous is highly scale dependent. In fact, it is inevitable that the damage distribution shows some degree of heterogeneity. By introducing a Gaussian distribution for microscale damage, our probabilistic damage model provides a quantitative micro-to-macro upscaling without mapping out the detailed locations where damage occurs. The good agreements between the model prediction and experimental data indicate that this model captures the overall effects of grain-scale microcracking, grain crushing and pore collapse on macro-scale permeability evolution.

5.6. Geological Applications

[60] The triaxial experiments of *Zhu et al.* [1997, 2002] show that the anisotropic development of permeability in lithified porous rocks is primarily controlled by stress. In contrast, at high strain, permeability and its anisotropic character are possibly controlled by the fabric development following cumulative strain. For instance, in the brittle faulting regime, large strain leads to the development of complex arrays of shear bands or the widening of shear bands [e.g., *Main et al.*, 2000]. Then, the overall permeability depends on the geometric complexity of the localized structures that evolve with cumulative strain. Strain is somewhat limited in a triaxial experimental configuration, which poses a serious limitation for studying the anisotropic development of permeability in unconsolidated materials such as sediments [*Dewhurst et al.*, 1996; *Bolton et al.*, 2000] and fault gouge [*Zhang et al.*, 1999, 2001]. In such settings, permeability is intimately related to the fabric of the sample, which evolves over very large strain. Recent experimental data from rotary shear tests on simulated gouge layers show that permeability for flow parallel to the shear directions can exceed the perpendicular component by one order of magnitude [*Zhang et al.*, 1999, 2001]. Such permeability anisotropy seems to persist over large shear strains on the order of 500 to 1000%, possibly due to the permanent alignment of clay minerals and Riedel shears along the shear direction [*Zhang et al.*, 1999, 2001]. Indeed, measurements on cores [*Faulkner and Rutter*, 1998] parallel and perpendicular to fault zones that have accumulated large strains corroborate this trend. It seems therefore that in unconsolidated materials such as sediments and fault gouge, the anisotropic development of permeability should be described by a model for the permeability tensor as a function of strain or slip. Such fundamental differences in evolution of permeability anisotropy should be accounted for in a crustal model that couples mechanical deformation and fluid transport. However, the widening of shear zones and development of an anastomosing network of shear bands at large strain [*Main et al.*, 2000] both involve failure of previously undamaged rock. Our experiments are therefore relevant for that the damage zone that surrounds active faults and dikes.

[61] The concept of a damage zone with stress-controlled damage surrounding a fault core with strain-controlled structure is consistent with the seismic anisotropy data of *Tadokoro et al.* [1999], who document fault-parallel fast S wave velocity direction within 500m of the Nojima fault rotating to parallel to the regional compressive stress direction at stations further than 1km for the fault. A similar structure can explain shear wave splitting measurements around the San Andreas Fault, with a $\sim$200m wide fault core [*Boness and Zoback*, 2006; *Cochran et al.*, 2006]. Our experimental results imply that the maximum principal permeability is along the direction of the most compressive stress in the damage zone. Accordingly, following *Zhang et al.* [2001], it is parallel to the shear direction in the fault core. In either case, maximum permeability is parallel to the seismically observed fast velocity direction. The effect of such a two-layer permeability structure of faults on fluid circulation should be explored. Permeability anisotropy in the damage zone would facilitate the evacuation of fluids away from faults, which may be important for the absence of a heat anomaly localized on the San Andreas Fault [*Saffer et al.*, 2003].

[62] Moreover, unlike in a natural system, healing is inefficient at the timescale of our deformation experiments. In contrast, fault healing is now well documented in the months to years that follow large earthquakes [e.g., *Li and Vidale*, 2001; *Li et al.*, 2006]. *Tadokoro and Ando* [2002] show a rotation of fast velocity direction in the fault core zone from fault-parallel to regional stress-parallel over 33 months following the 1995 Kobe earthquake. Fluid circulation is inferred from natural fault gouge microstructure to be dominantly coseismic [*Boullier et al.*, 2004]. This reflects healing of the strain-controlled microcracks but preservation of the stress-controlled microcracks. Thus after the long periods of interseismic inactivity, the fault gouge that is present at the initiation of a new earthquake, although strongly foliated, is probably healed. Rupture of gouge cement involves microcracking phenomena similar to those in our experiments. Therefore it is possible that rapid permeability evolution during earthquakes is similar to what we describe here. By contrast, earthquake dynamics simulations that take fluid pressurization into account have typically assumed constant or only porosity-dependent permeability [e.g., *Sleep and Blanpied*, 1992; *Andrews*, 2002; *Segall and Rice*, 2006]. It should be possible to adapt the probabilistic damage model presented here, which includes in particular a sharp permeability decreases upon a certain stress threshold, to coupled fluid flow and seismic rupture models. A similar probabilistic damage model captures the progressive development of foliation in a deforming polycrystalline aggregates [*Montési*, 2007].

[63] In summary, the transient permeability anisotropy with a permeability maximum in the most compressive stress direction, may be important in the damage zone that

surrounds fault cores and may even appears cyclically in the fault core due to diagenesis. Distributed low intensity strain is also present in the large-scale folds typical of deforming stratigraphic sequences. The hydrogeological implications of the abrupt permeability evolution and transient permeability anisotropy presented here need to be evaluated.

6. Conclusions

[64] Triaxial hydromechanical tests indicate that permeability and porosity evolution during shear-enhanced compaction is primarily controlled by stress. Furthermore, the influences of the mean effective stress and deviatoric stress can be separated. The drastic permeability reduction during shear-enhanced compaction is sensitive to the loading path, which indicates that the stress-induced permeability anisotropy may be significant in the cataclastic flow regime. Based on microstructural observations, we developed a probabilistic damage model to quantify stress-induced permeability anisotropy during the shear-enhanced compaction. Using this model, we are able to link the transient permeability anisotropy to the influence of stress state and loading path on the yield stress and microscopic stress heterogeneities. The good agreement between our modeling results and experimental data indicates that the probabilistic damage model provides a useful means to quantify the anisotropic reduction of permeability during cataclastic flow. While the development of permeability in lithified rocks is primarily controlled by microcracking and pore collapse, the evolution of permeability in unconsolidated materials, such as sediments and fault gouge, is primarily controlled by the development of fabric and shear localization via accumulation of shear strain. The fundamental differences in evolution of permeability anisotropy should be accounted for in crustal models that couple mechanical deformation and fluid transport.

[65] **Acknowledgments.** W.Z. was partially supported by the National Science Foundation under grants NSF-OCE0221436 and NSF-EAR 0510459, and the Department of Energy under grant #DEFGO200ER15058 (WHOI). LM was supported by the National Science Foundation under grant NSF-EAR0337678.

References

Andrews, D. J. (2002), A fault constitutive relation accounting for thermal pressurization of pore fluid, *J. Geophys. Res.*, *107*(B12), 2363, doi:10.1029/2002JB001942.

Baud, P., W. Zhu, and T.-f. Wong (2000), Failure mode and weakening effect of water on sandstone, *J. Geophys. Res.*, *105*, 16,371–16,389.

Baud, P., V. Vajdova, and T.-f. Wong (2006), Shear-enhanced compaction and strain localization: Inelastic deformation and constitutive modeling of four porous sandstones, *J. Geophys. Res.*, *111*, B12401, doi:10.1029/2005JB004101.

Bernabé, Y. (1987), A wide range permeameter for use in rock physics, *Int. J. Rock Mech. Min. Sci.*, *24*, 309–315.

Bernabé, Y., U. Mok, and B. Evans (2003), Permeability-porosity relationships in rocks subjected to various evolution processes, *Pure Appl. Geophys.*, *160*(5–6), 937–960.

Bésuelle, P. (2001), Compacting and Dilating shear bnads in porous rock, *J. Geophys. Res.*, *106*, 13,435–13,442.

Bolton, A. J., A. J. Maltman, and Q. Fisher (2000), Anisotropic permeability and bimodal pore-size distributions of fine-grained marine sediments, *Mar. Pet. Geol.*, *17*, 657–672.

Boness, N. L., and M. D. Zoback (2006), Mapping stress and structurally controlled crustal shear velocity anisotropy in California, *Geology*, *34*, 825–828, doi:10.1130/G22309.1.

Boullier, A.-M., K. Fujimoto, H. Ito, T. Ohtani, N. Keulen, O. Fabbri, D. Armitrano, M. Dubois, and P. Pezard (2004), Structural evolution of the Nojima fault (Awaji Island, Japan) revisited from GSJ drill hole at Hirabayashi, *Earth Planets Space*, *56*, 1233–1240.

Bourbie, T., and B. Zinszner (1985), Hydraulic and acoustic properties as a function of porosity in Fontainebleau sandstone, *J. Geophys. Res.*, *90*(13), 11,524–11,532.

Brace, W. F. (1980), Permeability of crystalline and argillaceous rocks, *Int. J. Rock Mech. Min. Sci.*, *17*, 241–251.

Bruno, M. S. (1994), Micromechanics of stress-induced permeability anisotropy and damage in sedimentary rock, *Mech. Mater.*, *18*, 31–48.

Cochran, E. S., Y.-G. li, and J. E. Vidale (2006), Anisotropy in the shallow crust observed around the San Andreas Fault before and after the 2004 M 6.0 Parkfield Earthquake, *Bull. Seismol. Soc. Am.*, *96*, S364–S375, doi:10.1785/0120050804.

David, C., T.-f. Wong, W. Zhu, and J. Zhang (1994), Laboratory measurement of compaction-induced permeability change in porous rock: implications for the generation and maintenance of pore pressure excess in the crust, *Pure Appl. Geophys.*, *143*, 425–456.

Dewhurst, D. N., M. B. Clennell, K. M. Brown, and G. K. Westbrook (1996), Fabric and hydraulic conductivity of shear clays, *Geotechnique*, *46*, 761–768.

DiMaggio, F. L., and I. S. Sandler (1971), Material model for granular soils, *J. Engineering Mechanics*, American Soc. of Civil Eng., *97*, 935–950.

Faulkner, D. R., and E. H. Rutter (1998), The gas permeability of clay-bearing fault gouge at 20°C, in: *Faults, Fault Sealing and Fluid Flow in Hydrocarbon Reservoirs*, edited by G. Jones, Q. Fisher, and R. J. Knipe, Geological Society, Special Publications, London, 147–156.

Fortin, J., A. Schubnel, and Y. Guéguen (2005), Elastic wave velocities and permeability evolution during compaction of sandstone, *International J. Rock Mechanics*, *42*, 873–889.

Fortin, J., S. Stanchits, G. Dresen, and Y. Guéguen (2006), Acoustic emission and velocities associated with the formation of compaction bands in sandstone, *J. Geophys. Res.*, *111*, B10203, doi:10.1029/2005JB003854.

Fredrich, J. T., B. Menéndez, and T.-f. Wong (1995), Imaging the pore structure of geomaterials, *Science*, *268*, 276–279.

Gallagher, J. J., M. Friedman, J. Handin, and G. Sowers (1974), Experimental studies relating to microfracture in sandstone, *Tectonophysics*, *21*, 203–247.

Gangi, A. F. (1979), Variation of whole and fractured porous rock permeability with confining pressure, *Int. J. Rock Mech. Min. Sci. & Geomechanical Abstracts*, *15*, 249–257.

Grueschow, E., and J. Rudnicki (2005), Elliptic yield cap constitutive modeling for high porosity sandstone, *Int. J. Solids Struct.*, *42*, 4574–4587, doi:10.1016/j.ijsolstr.2005.02.001. (http://www.sciencedirect.com/science/journal/00207683; http://dx.doi.org/10.1016/j.ijsolstr.2005.02.001)

Heard, H. C., and L. Page (1982), Elastic moduli, thermal expansion and inferred permeability of two granites to 350°C and 55 MPa, *J. Geophys. Res.*, *87*, 9340–9348.

Holt, R. M. (1989), Permeability reduction induced by a nonhydrostatic stress field, *Proc. Annu. Tech. Conf. Exhib. Soc. Petroleum Eng. of AIME*, *64*, SPE19595.

Ingebritsen, S. E., and W. E. Sanford (1998), *Groundwater in Geologic Processes*, Cambridge Univ. Press, New York, 341.

Kiyama, T., H. Kita, Y. Ishijima, T. Yanagidani, K. Aoki, and T. Sato (1996), Permeability in anisotropic granite under hydrostatic compression and triaxial compression including post-failure region, *Proc. North Am. Rock Mech. Symp.*, *2*, 1161–1168.

Li, Y.-G., and J. E. Vidale (2001), Healing of the shallow fault zone from 1994–1998 after the 1992 M7.5 Landers, California, earthquake, *Geophys. Res. Lett.*, *28*, 2999–3002.

Li, Y.-G., P. Chen, E. S. Cochran, J. E. Vidale, and T. Burnette (2006), Seismic Evidence for rock damage and healing on the San Andreas fault associated with the 2004 M 6.0 Parkfield earthquake, *Bull. Seismol. Soc. Am.*, *96*, S349–S363, doi:10.1785/0120050803.

Lockner, D. A., J. D. Byerlee, V. Kuksenko, A. Ponomarev, and A. Sidorin (1992), Observations of quasistatic fault growth from acoustic emissions, in: *Fault Mechanics and Transport Properties of Rocks*, edited by B. Evans and T.-f. Wong, Academic Press, San Diego, 1-31.

Madden, T. R. (1976), Random networks and mixing laws, *Geophysics*, *41*, 1104–1125.

Main, I. G., O. Kwon, B. T. Ngwenya, and S. C. Elphick (2000), Fault sealing during deformation band growth in porous sandstone, *Geology*, *28*, 1131–1134.

Main, I. G., K. Mair, O. Kwon, S. Elphick, and B. Ngwenya (2001), Recent experimental constraints on the mechanical and hydraulic properties of deformation bands in porous sandstones: a review, In: *The nature and significance of fault zone weakening*, edited by R. E. Holsworth, R. A. Strachan, J. F. Magloughlin, and R. J. Knipe, Geological Soc. of London, Special Publications, *186*, p43–63.

Menéndez, B., W. Zhu, and T.-f. Wong (1996), Micromechanics of brittle faulting and cataclastic flow in Berea sandstone, *J. Struct. Geol.*, *18*, 1–16.

Menéndez, B., C. David, and A. Martinez Nistal (2001), Confocal scanning laser microscopy applied to the study of void networks in cracked granite samples and in cemented sandstones, *Comput. Geosci.*, *27*, 1101–1109.

Mogi, K. (1968), Effects of the intermediate principal stress on rock failure, *J. Geophys. Res.*, *72*, 5117–5131.

Montési, L. G. J. (2007), A constitutive model for the development of foliation near the brittle-ductile transition, submitted to, *Geophys. Res. Lett.*, *34*, L08307, doi:10.1029/2007GL029250.

Mordecai, M., and L. H. Morris (1971), An investigation into the changes of permeability occurring in a sandstone when failed under triaxial stress conditions, *Proc. 12th U. S. Symp. Rock Mech.*, *12*, 221–239.

Morris, J. P., I. N. Lomov, and L. A. Glenn (2003), A constitutive model for stress-induced permeability and porosity evolution of Berea sandstone, *J. Geophys. Res.*, *108*(B10), 2252, doi:10.1029/2001JB000463.

Ngwenya, B. T., O. Kwon, S. C. Elphick, and I. Main (2003), Permeability evolution during progressive development of deformation bands in porous sandstones, *J. Geophys. Res.*, *108*(B7), 2343, doi:10.1029/2002JB001854.

Paterson, M. S. (1983), The equivalent channel model for permeability and resistivity in fluid-saturated rock-A re-appraisal, *Mech. Mater.*, *2*, 345–352.

Peach, C. J., and C. J. Spiers (1996), Influence of crystal plastic deformation on dilatancy and permeability development in synthetic salt rock, *Tectonophysics*, *256*, 101–128.

Person, M., J. P. Raffensperger, S. Ge, and G. Garven (1996), Basin-scale hydrogeologic modeling, *Rev. Geophys.*, *34*, 61–87.

Rhett, D. W., and L. W. Teufel (1992), Stress path dependence of matrix permeability of North Sea sandstone reservoir rock, *Proc. 33rd U. S. Symp. Rock Mech.*, *33*, 345–354.

Saffer, D. M., B. A. Bekins, and S. Hickman (2003), Topographically driven groundwater flow and the San Andreas heat flow paradox revisited, *J. Geophys. Res.*, *108*(B5), 2274, doi:10.1029/2002JB001849.

Schofield, A. N., and C. P. Wroth (1968), Critical state soil mechanics. McGraw Hill, London, 310.

Segall, P., and J. R. Rice (2006), Does shear heating of pore fluid contribute to earthquake nucleation?, *J. Geophys. Res.*, *111*, B09316, doi:10.1029/2005JB004129.

Shankland, T. J., R. J. O'Connell, and H. S. Waff (1981), Geophysical constraints on partial melt in the upper mantle, *Rev. Geophys. Space Phys.*, *19*, 394–406.

Simmons, G., and D. Richter (1976), Microcracks in rocks, in *The Physics and Chemistry of Minerals and Rocks*, edited by R. G. J. Sterns, pp. 105–137, Wiley-Interscience, New York.

Sleep, N. H., and M. L. Blanpied (1992), Creep, compaction and the weak rheology of major faults, *Nature*, *359*, 687–692.

Stormont, J. C., and J. J. K. Daemen (1992), Laboratory study of gas permeability changes in rock salt during deformation., *Int. J. Rock Mech. Min. Sci.*, *29*, 323–342.

Tadokoro, K., and M. Ando (2002), Evidence for rapid fault healing derived from temporal changes in S wave splitting, *Geophys. Res. Lett.*, *29*(4), 1047, doi:10.1029/2001GL013644.

Tadokoro, K., M. Ando, and Y. Umeda (1999), S wave splitting in the aftershock region of the 1995 Hyogo-ken Nanbu earthquake, *J. Geophys. Res.*, *104*(B1), 981–991.

Walsh, J. B. (1965), The effect of cracks on the compressibility of rock, *J. Geophys. Res.*, *70*, 381–389.

Walsh, J. B., and W. F. Brace (1984), The effect of pressure on porosity and the transport properties of rock, *J. Geophys. Res.*, *89*, 9425–9431.

Wong, T.-f., and W. Zhu (1999), Brittle faulting and permeability evolution: hydromechanical measurement, microstructural observation, and network modeling, in: *Faults & Subsurface Fluid Flow in the Shallow Crust*, AGU Geophysical Monograph, *113*, 83–99.

Wong, T.-f., H. Szeto, and J. Zhang (1992), Effect of loading path and porosity on the failure mode of porous rocks, *Appl. Mech. Rev.*, *45*, 281–293.

Wong, T.-f., C. David, and W. Zhu (1997), The transition from brittle faulting to cataclastic flow in porous sandstones: Mechanical deformation, *J. Geophys. Res.*, *102*, 3009–3025.

Zhang, J., T.-f. Wong, T. Yanagidani, and D. M. Davis (1990), Pressure-induced microcracking and grain crushing in Berea and Boise sandstones: Acoustic emission and quantitative microscopy measurements, *Mech. Mater.*, *9*, 1–15.

Zhang, S., S. F. Cox, and M. S. Paterson (1994), The influence of room temperature deformation on porosity and permeability in calcite aggregates, *J. Geophys. Res.*, *99*, 15,761–15,775.

Zhang, S., T. E. Tullis, and V. J. Scruggs (1999), Permeability anisotropy and pressure dependency of permeability in experimentally sheared gouge materials, *J. Struct. Geol.*, *21*, 795–806.

Zhang, S., T. E. Tullis, and V. J. Scruggs (2001), Implications of permeability and its anisotropy in a mica gouge for pore pressures in fault zones, *Tectonophysics*, *335*, 37–50.

Zhu, W. (2006), Quantitative characterization of permeability reduction associated with compactive cataclastic flow, in: *Radiated energy and the physics of earthquake faulting*, AGU Monograph, in press.

Zhu, W., and T.-f. Wong (1997), The transition from brittle faulting to cataclastic flow: Permeability evolution, *J. Geophys. Res.*, *102*, 3027–3041.

Zhu, W., and T.-f. Wong (1999), Network modeling of the evolution of permeability and dilatancy in compact rocks, *J. Geophys. Res.*, *104*, 1963–2971.

Zhu, W., L. G. J. Montési, and T.-f. Wong (1997), Shear-enhanced compaction and permeability reduction: Triaxial extension tests on porous sandstone, *Mech. Mater.*, *25*, 199–214.

Zhu, W., L. G. J. Montési, and T.-f. Wong (2002), Effects of stress on the anisotropic development of permeability during mechanical compaction of porous sandstones, in: *Deformation Mechanisms, Rheology and Tectonics*: *Current Status and Future Perspectives*, edited by S. Meer, M. R. Drury, de J. H. P. de Bresser, and G. M. Pennock, Geological Society, London, Special Publications, *200*, 119–136.

Zoback, M. D., and J. D. Byerlee (1975), The effect of microcrack dilatancy on the permeability of Westerly granite, *J. Geophys. Res.*, *80*, 752–755.

Zoback, M. D., and J. D. Byerlee (1976), Effect of high-pressure deformation on permeability of Ottawa Sand, *Am. Assoc. Petrol. Geol. Bull.*, *60*, 1531–1542.

L. G. J. Montési and W. Zhu, Department of Geology and Geophysics, Woods Hole Oceanographic Institution, Woods Hole, MA 02543, USA. (wzhu@whoi.edu)

T.-f. Wong, Department of Geosciences, State University of New York at Stony Brook, Stony Brook, NY 11794, USA.